Optics & Laser Technology 202 (2026) 115399

Contents lists available at ScienceDirect

Optics and Laser Technology

journal homepage: www.elsevier.com/locate/jolt

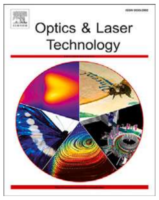

Full length article

Plasmonically assisted coherent control of photonic spin hall shifts

Muqaddar Abbas[a], Spyridon G. Kosionis[b], Vassilios Yannopapas[c], Emmanuel Paspalakis[b], Hamid R. Hamedi[d,*]

[a] *Department of Foundation Teaching and Research, Shenyang Urban Construction University, Shenyang, 110167, China*
[b] *Materials Science Department, School of Natural Sciences, University of Patras, Patras 265 04, Greece*
[c] *Department of Physics, School of Applied Mathematical and Physical Sciences, National Technical University of Athens, Athens 157 80, Greece*
[d] *Institute of Theoretical Physics and Astronomy, Vilnius University, Sauletekio 3, Vilnius 10257, Lithuania*

ARTICLE INFO

Keywords:
Photonic spin Hall shifts
Electromagnetically induced transparency
V-type quantum system
Plasmonic nanostructure

ABSTRACT

We investigate coherent control of photonic spin Hall shifts in a hybrid platform where a quantum emitter layer is placed in the near field of a plasmonic nanostructure supporting surface plasmon polaritons. The hybridization produces a plasmon-induced transparency that reshapes the polarization-dependent reflection of a multilayer cavity. Two control parameters, the imbalance between the s- and p-polarized reflection channels and the angular variation of the p-polarized reflection phase, govern both the magnitude and sign of the spin-dependent transverse displacement. Beyond the linear regime, nonlinear optical response arising from the third-order susceptibility introduces an intensity-dependent correction that modifies the angular phase dispersion and shifts the sign-transition angle of the displacement. By tuning the probe detuning, driving strength, and emitter–metal separation, we predict large, sign-reversible photonic spin Hall shifts near the surface-plasmon coupling angle, with angle-detuning maps revealing a thin control ridge for deterministic polarity switching. The scheme is in principle compatible with on-chip integration and may be promising for room-temperature implementations.

1. Introduction

Electromagnetically induced transparency (EIT) offers a powerful means of tailoring optical dispersion and absorption through quantum interference in multilevel media, producing narrow transparency windows together with steep normal dispersion and greatly reduced group velocity [1]. When such interference effects are engineered in the near field of metallic nanostructures that support surface plasmon polaritons (SPPs), the local density of optical states and radiative pathways can be dramatically reshaped, providing new ways to control light-matter coupling at deeply subwavelength scales [2]. Interference between bright and dark optical pathways, closely related to Fano resonances in plasmonic systems [3], can then be used to reproduce EIT-like line shapes and slow-light behavior in nanoscale environments [4,5]. Recent studies of plasmon-induced transparency (PIT) in hybrid 2D-material nanostructures and terahertz semiconductor plasmonic waveguides further illustrate the breadth of transparency-based control in nanophotonics [6,7].

In this context, a four-level quantum emitter placed near a plasmonic nanostructure has been shown to produce transparency and slow light through the interplay between quantum interference and plasmon-enhanced decay channels [8]. That study identified parameter regimes in which the emitter-nanostructure distance modifies both the absorption profile and the group index, enabling tunable transparency windows and controllable group delays in a geometry compatible with integrated nanophotonics. By varying detunings and relaxation rates relevant to the emitter–plasmon hybrid, one can balance plasmonic losses and Purcell-enhanced decay with coherent driving to restore transparency while retaining large dispersion, a prerequisite for slow-light applications.

Since this pioneering work, the same type of quantum emitter–plasmonic nanostructure hybrid has been used to study a range of coherent optical phenomena, including modified spontaneous emission [9], controlled absorption [10], spatially structured optical effects [11,12], patterned light amplification without inversion [13], spatially patterned spontaneous emission [14], and enhanced Kerr nonlinearity [15,16], as well as optical bistability [17]. More broadly, the merging of quantum-optical interference with plasmonic confinement opens the design space for on-chip delay lines, narrowband filtering, and enhanced nonlinear optics at low photon numbers [1–5].

The same subwavelength structuring and strong field gradients that enable EIT-like interference in plasmonic environments also enhance spin–orbit interactions of light. Beyond dispersion engineering, one can

---

* Corresponding author.
Email addresses: muqaddarabbas@outlook.com (M. Abbas), kosionis@upatras.gr (S.G. Kosionis), vyannop@mail.ntua.gr (V. Yannopapas), paspalak@upatras.gr (E. Paspalakis), hamid.hamedi@tfai.vu.lt (H.R. Hamedi).

https://doi.org/10.1016/j.optlastec.2026.115399
Received 19 March 2026; Received in revised form 19 April 2026; Accepted 22 April 2026

therefore exploit polarization-trajectory coupling to control beam shifts and transverse momentum flow at interfaces and in inhomogeneous media [18]. This motivates the present study, which explores a complementary mechanism for beam control based on spin–orbit physics.

The photonic spin Hall effect (PSHE) is a representative example of spin–orbit coupling in optics: a light beam acquires a polarization-dependent transverse shift when it encounters gradients or discontinuities in refractive index [19]. This displacement reflects the coupling between a photon's spin angular momentum (its polarization) and the trajectory of its wavefront, serving as an optical counterpart to the spin Hall effect known from electronic systems [18]. In this analogy, spatial variations of the dielectric environment play the role of effective fields that generate opposite lateral shifts for the two circular polarization components [19–21].

Foundational theory by Onoda et al. established the basic mechanism and predicted measurable beam shifts [19], while subsequent work by Bliokh and coauthors connected these effects to conservation laws and geometric phase [20]. A comprehensive overview of the underlying Goos-Hänchen and Imbert-Fedorov beam-shift physics is given in Ref. [22]. A decisive experimental milestone was achieved by Hosten and Kwiat, who employed weak measurement techniques to amplify and directly resolve the tiny polarization-induced deflections at an interface [23], and Zhou et al. subsequently demonstrated the spin Hall effect of light on a nanometal film using weak measurements [24].

At a fundamental level, PSHE expresses the conservation of total angular momentum in light-matter interactions, making it a sensitive probe of spin–orbit physics in structured and inhomogeneous media [18,25]. Weak-value-based metrology has become a standard tool for detecting these subwavelength shifts with high precision [26,27]. As a result, PSHE underpins a growing range of applications from precision sensing and quantum photonics to advanced imaging, where spin-dependent beam steering and enhanced displacement sensitivity serve as key performance enablers [28–30]. Recent comprehensive reviews cover the theory, manipulation, and emerging applications of PSHE [31–33], while new platforms based on metasurfaces [34], surface plasmon resonance [35–42], quantum wells [43], quantum dot molecules [44], and cavity magnomechanical systems [45] continue to extend the scope and controllability of PSHE. Flexible coherent control of plasmonic spin-Hall shifts has also been demonstrated [46].

In addition, recent application-oriented studies have demonstrated PSHE enhancement and sensing functionality in $\mathrm{BaTiO_3}$-based plasmonic platforms, piezoplasmonic structures for refractive-index sensing, anisotropic black-phosphorus systems for $\mathrm{NO_2}$ detection, silicon-waveguide plasmonic magnetic-field sensors, and graphene-assisted near-infrared plasmonic sensors, further highlighting the versatility of PSHE-enabled nanophotonic and sensing devices [47–51].

While PSHE has been explored across various photonic architectures, a quantum emitter operating in the near field of a plasmonic nanostructure offers a powerful and still underexploited route to spin–orbit photonics. Plasmonic modes supply extreme field confinement and large optical density of states, which in turn enhance light-matter coupling, accelerate radiative channels via the Purcell effect, and generate steep spatial gradients that strengthen spin–orbit interactions of light [2,18,52,53]. In contrast to purely dielectric platforms (metasurfaces, photonic crystals) or dilute atomic media, the emitter–plasmon hybrid combines a nanoscale footprint with dispersion control through interference (EIT- and plasmonically induced transparency-like responses) and broadband geometry-based tunability [1,3,4].

Beyond their linear optical response, quantum-plasmonic systems can also exhibit modified nonlinear susceptibilities. In particular, a nearby plasmonic nanostructure can give rise to an effective third-order nonlinear response in multilevel emitters, whose strength depends sensitively on the emitter–metal separation and on plasmon-controlled decay channels [15,16,54]. Such behavior provides an intensity-dependent mechanism for influencing the optical dispersion and refractive index experienced by a probe field, opening the possibility of actively tuning interference-based optical effects through the probe intensity itself.

Building on these advantages, we focus on a regime in which a weak probe field interacts coherently with a hybrid quantum emitter layer, thereby tailoring the complex susceptibility seen by the probe. By varying the emitter-surface separation, the hybrid structure reshapes both absorption and dispersion, enabling amplification or suppression of spin-dependent lateral shifts with a programmable sign and magnitude. In this framework, the same interference mechanisms that give rise to plasmon-assisted transparency and slow light [8] provide a practical means to control the PSHE: interference restores transparency and reduces loss, while the engineered dispersion profile exploits the coupling between polarization and trajectory to generate large, tunable beam displacements [18–20].

Several recent works have explored the control of PSHE using atomic coherence effects. Wan and Zubairy proposed controlling the photonic spin Hall shift via surface plasmon resonance with an N-type coherent medium [55]. Wu et al. studied spin Hall shifts in multilevel atomic systems [56]. More recently, Waseem et al. demonstrated gain-assisted control of the PSHE [57], and Abbas et al. investigated tunable PSHE in tripod configurations [58] and through vacuum-induced transparency in an atomic cavity [59]. The PSHE has also been explored in cavity magnomechanical systems [45] and coherent control schemes in cavity QED [60].

In contrast to earlier coherence-controlled PSHE schemes based on vacuum-induced transparency in atomic cavities [59] and double-tunneling-induced transparency in quantum dot molecules [61], the present work considers a hybrid quantum-emitter–plasmonic cavity in which the relevant interference mechanism is plasmon-induced transparency generated by near-field coupling to a plasmonic nanoshell array. This platform introduces plasmonically modified decay channels, Purcell-enhanced anisotropy, and emitter–metal separation as physically distinct control parameters for the PSHE. In addition, the present formulation identifies the reflection-channel imbalance and the angular phase dispersion of the TM reflection coefficient as the two compact quantities governing the magnitude and sign reversal of the transverse shift, and extends the analysis beyond the linear regime through an effective third-order susceptibility. Taken together, these features distinguish the present scheme from earlier coherence-controlled PSHE platforms based on purely atomic or semiconductor interference mechanisms.

Operationally, the proposed platform is in principle compatible with on-chip integration and may be adaptable to room-temperature operation through suitable material and geometrical design. At the same time, the present work should be viewed as a proof-of-principle theoretical study based on an idealized hybrid structure. A realistic device-level assessment would require explicit treatment of fabrication tolerances, structural disorder, surface roughness, emitter-position fluctuations, pure dephasing, inhomogeneous broadening, and additional nonradiative loss channels. These effects, together with experimental validation, are beyond the scope of the present work and are left for future investigation. Within these scope limitations, our aim here is to establish the underlying physical mechanism and the main control trends by which plasmon-assisted interference and nonlinear tunability can be used to manipulate the PSHE in hybrid nanophotonic structures.

2. Theoretical model and physical configuration

We investigate a hybrid cavity-plasmonic structure using both an effective cavity description and a microscopic model. In the effective picture, the device is composed of three layers: two outer mirrors with permittivities ϵ_1 and ϵ_3 with thickness d_1, and a central active region of thickness d_2 described by the effective permittivity $\epsilon_2 = 1 + \chi_{\mathrm{eff}}$. The input mirror M_1 is partially reflecting, while the second mirror M_2 forms the output side of the resonator. The polarization-dependent reflection coefficients relevant to the PSHE are determined by the optical response of this intermediate effective medium.

From the microscopic viewpoint, the susceptibility χ_{eff} originates from a quantum-emitter layer positioned in vacuum at a distance d from a plasmonic nanostructure. Near-field coupling between the emitters and the plasmonic element modifies the emitter response and, in turn, the effective optical properties of the central layer. The structure is driven by a weak probe field of frequency ω_p, incident on M_1 at an angle θ_{i}. The probe contains both transverse-electric (TE) and transverse-magnetic (TM) components.

When the probe reflects from the three-layer cavity, its left- and right-circularly polarized components undergo different phase and amplitude variations. As a result, the reflected beam exhibits a transverse out-of-plane spin-dependent separation, which is a characteristic manifestation of the PSHE, as shown in Fig. 1(a). The mechanism underlying this effect and its relation to the multilayer configuration are discussed below.

2.1. Photonic spin hall effect: concept and working formulas

For the three-layer cavity configuration, the TE (s) and TM (p) reflection coefficients obtained via the transfer-matrix formalism are given by

$$R_{p,s} = \frac{R_{12,p,s} + R_{23,p,s}\, e^{2ik_{2z}q}}{1 + R_{12,p,s}R_{23,p,s}\, e^{2ik_{2z}q}}, \tag{1}$$

where q denotes the thickness of the intermediate (cavity) layer, and $R_{12,p/s}$ ($R_{23,p/s}$) represent the reflection coefficients at the mirror 1/medium (medium/mirror 2) interfaces, respectively. For a single interface between media i and j, the Fresnel coefficients are

$$R_{ij,p} = \frac{\epsilon_j k_{iz} - \epsilon_i k_{jz}}{\epsilon_j k_{iz} + \epsilon_i k_{jz}}, \qquad R_{ij,s} = \frac{k_{iz} - k_{jz}}{k_{iz} + k_{jz}}. \tag{2}$$

Here, the normal components of the wavevector are $k_{iz} = \sqrt{k_0^2\epsilon_i - k_x^2}$, with $k_x = \sqrt{\epsilon_1}\, k \sin\theta_i$, and $k = 2\pi/\lambda$ is the wave vector in vacuum.

From Eq. (1), it follows that the effective reflection coefficients $R_{p,s}$ depend on the permittivity of the cavity medium, ϵ_2, which is governed by its susceptibility χ. The dispersive properties of the intracavity material therefore provide a convenient means to tailor the PSHE response. In the present work, the intracavity permittivity is written as $\epsilon_2 = 1 + \chi_{\mathrm{eff}}$, where χ_{eff} is the effective susceptibility of the plasmon-coupled quantum-emitter layer described in Section 2.2. This effective-medium description is used in the cavity transfer-matrix model, while the dependence on the emitter-plasmon separation d enters through χ_{eff}.

For a localized TM-polarized Gaussian probe, the reflected left- and right-handed circular fields can be written as

$$\mathcal{E}_r^{\pm}(x_r, y_r, z_r) = \frac{w_0}{w}\, \exp\left[-\frac{x_r^2 + y_r^2}{w^2}\right] \times \left[R_p - \frac{2i\, x_r}{k\, w}\, \frac{\partial R_p}{\partial \theta_i} \mp \frac{2\, y_r \cot\theta_i}{k\, w}\, (R_s + R_p)\right], \tag{3}$$

where $w = w_0[1 + (2z_r/k_1 w_0^2)^2]^{1/2}$, $z_r = k_1 w_0^2/2$ denotes the Rayleigh length. Here, w_0 is the waist radius of the incident beam, (x_r, y_r, z_r) denotes the coordinate system of the reflected field, and the superscript $\pm$ distinguishes the two spin states. In addition, $k_1 = \sqrt{\epsilon_1}\, k$. Then, the transverse shift of the reflected beam is given by

$$\delta_{p\pm} = \frac{\int y \left|\mathcal{E}_r^{\pm}(x_r, y_r, z_r)\right|^2 dx_r\, dy_r}{\int \left|\mathcal{E}_r^{\pm}(x_r, y_r, z_r)\right|^2 dx_r\, dy_r}, \tag{4}$$

which, after inserting Eq. (3), yields

$$\delta_{p\pm} = \mp \frac{k_1\, w_0^2\, \mathrm{Re}\left[1 + \frac{R_s}{R_p}\right] \cot\theta_i}{k_1^2 w_0^2 + \left|\frac{\partial \ln R_p}{\partial \theta_i}\right|^2 + \left|\left(1 + \frac{R_s}{R_p}\right) \cot\theta_i\right|^2}. \tag{5}$$

By symmetry, δ_{p+} and δ_{p-} have the same magnitude and opposite signs. Here it is useful to distinguish the present observable from other standard beam shifts. The Goos-Hänchen (GH) shift is an in-plane longitudinal displacement of the reflected beam centroid along the plane of incidence, usually associated with the angular derivative of the reflection phase for a given polarization channel. By contrast, the Imbert-Fedorov (IF) shift is a transverse displacement perpendicular to the plane of incidence and originates from spin–orbit coupling of light through the coupled amplitude-phase response of the polarization channels. The PSHE studied in the present work corresponds to this transverse IF-type spin splitting, in which the left- and right-circular components acquire opposite transverse displacements. By contrast, so-called in-plane PSHE refers to a different type of spin-dependent separation within

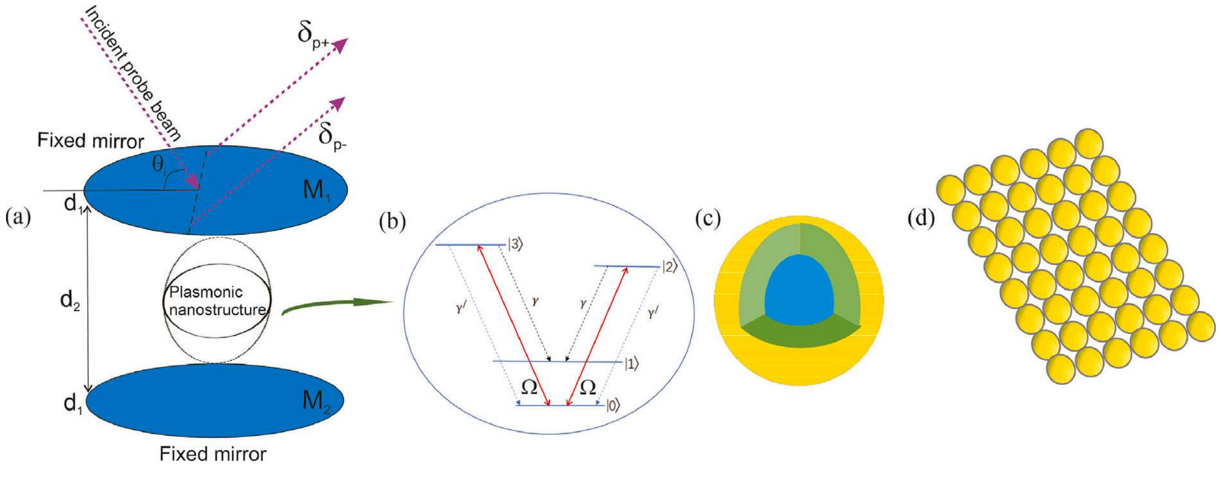

Fig. 1. (a) Planar three-layer cavity bounded by mirrors M_1 and M_2, whose central layer is modeled as an effective active medium with permittivity $\epsilon_2 = 1 + \chi_{\mathrm{eff}}$. The effective susceptibility χ_{eff} is obtained from the plasmon-coupled quantum-emitter layer described in Section 2.2 and is used to represent the active intracavity response. The quantities δ_{p+} and δ_{p-} denote the transverse displacements of the reflected probe for left- and right-circular polarizations, respectively. (b) Energy-level scheme of the double-V system, where the probe simultaneously addresses the $|0\rangle \leftrightarrow |3\rangle$ and $|0\rangle \leftrightarrow |2\rangle$ transitions. (c) Metal-coated dielectric nanosphere. (d) Two-dimensional lattice of such nanospheres.

the plane of incidence, which can arise in more anisotropic or specially engineered optical systems. The present theory and all reported numerical results are therefore restricted to the transverse, out-of-plane IF-type PSHE.

Eq. (5) makes explicit the dependence of the PSHE on the Fresnel ratio R_s/R_p and on the angular derivative $\partial_{\theta_i} \ln R_p$. To make this dependence more transparent, we note that

$$\frac{\partial \ln R_p}{\partial \theta_i} = \frac{1}{|R_p|}\frac{\partial |R_p|}{\partial \theta_i} + i\,\frac{\partial \arg(R_p)}{\partial \theta_i}. \tag{6}$$

While no separate plot of $\arg(R_p)$ is provided, Eq. (6) makes clear that the PSHE depends on the full complex angular response of R_p, and the observed offset between the reflection minimum and the PSHE extrema is consistent with a non-negligible phase-gradient contribution. Hence, the PSHE is governed by the full complex angular response of the TM reflection coefficient, with contributions arising from both amplitude variation and phase gradient [22]. Physically, the ratio R_s/R_p measures the imbalance between the TE and TM reflection channels. When this imbalance becomes stronger, the reflected field acquires a larger spin-dependent asymmetry, and the transverse splitting is correspondingly enhanced. By contrast, $\partial_{\theta_i} \ln R_p$ measures how sensitively the complex TM reflection coefficient responds to the incidence angle. Its real part describes the angular variation of the reflection amplitude, while its imaginary part describes the angular phase gradient. The latter becomes especially important near resonance, where the phase of R_p varies rapidly with angle.

The two quantities therefore play distinct but complementary roles. The reflection-channel imbalance sets the overall strength of the spin-dependent response, whereas the angular phase dispersion determines the angular region where the displacement is most strongly enhanced and where its sign can reverse. For this reason, the sign-transition region is generally found near the TM reflection minimum, while the largest positive and negative PSHE extrema occur at nearby angles where the polarization imbalance and phase-sensitive enhancement act together most effectively. In our hybrid cavity-plasmonic platform, both quantities are tunable through the effective intracavity permittivity $\epsilon_2 = 1 + \chi_{\text{eff}}$. Two compact control parameters therefore govern the PSHE: the ratio R_s/R_p and the angular dispersion $\partial_{\theta_i} \ln R_p$.

Unlike most PSHE implementations, such as planar reflections, static metasurfaces, or weak-measurement arrangements, which function as passive elements, our cavity-quantum-emitter-plasmonic hybrid provides an actively controllable pathway. Here the probe susceptibility χ_{eff} modulates the intracavity permittivity ϵ_2, which in turn tailors the Fresnel responses $R_{s,p}$ and their angular dispersion that govern Eq. (5). Through this mechanism, PSHE can be tuned in real time by adjusting system parameters and the emitter-plasmon separation, opening operating points and dynamical protocols that passive optics cannot access.

Our analysis uses the paraxial, small-displacement approximation for a Gaussian probe. Material dispersion is captured by $\chi_{\text{eff}}(\delta)$ derived in Section 2.2. Under the parameters considered, higher-order spatial and nonparaxial corrections are negligible.

2.2. *Quantum system and optical susceptibility*

The quantum system under study [Fig. 1(b)] is a four-level, double-V configuration with two closely spaced excited states $|2\rangle$ and $|3\rangle$ and two lower states $|0\rangle$ and $|1\rangle$. This labeling makes it clear that two distinct three-level V subsystems are embedded in the structure. Topologically, the scheme is also equivalent to a double-Λ system. The emitter layer is placed in vacuum at a distance d from a plasmonic nanostructure, and the resulting plasmon-modified decay rates and coherence parameters determine the effective susceptibility χ_{eff} entering the cavity model. We take $|2\rangle$ and $|3\rangle$ to represent two Zeeman sublevels.

The dipole operator is chosen as

$$\boldsymbol{\mu} = \mu\big(|2\rangle\langle 0|\,\hat{\boldsymbol{\varepsilon}}_- + |3\rangle\langle 0|\,\hat{\boldsymbol{\varepsilon}}_+ + |2\rangle\langle 1|\,\hat{\boldsymbol{\varepsilon}}_- + |3\rangle\langle 1|\,\hat{\boldsymbol{\varepsilon}}_+\big) + \text{H.c.}, \tag{7}$$

where the circular unit vectors are $\hat{\boldsymbol{\varepsilon}}_\pm = (\hat{\mathbf{z}} \pm i\hat{\mathbf{x}})/\sqrt{2}$. For simplicity, the dipole amplitudes are taken to be real.

A linearly polarized, continuous-wave probe field drives the transitions $|0\rangle \leftrightarrow |2\rangle, |3\rangle$:

$$\mathbf{E}(t) = \hat{\mathbf{z}}\, E_p \cos(\omega_p t), \tag{8}$$

with amplitude E_p and angular frequency ω_p. Within the dipole and rotating-wave approximations, the system Hamiltonian reads

$$\begin{aligned} H = {} & \hbar\Big(-\delta - \frac{\omega_{32}}{2}\Big)|2\rangle\langle 2| + \hbar\Big(-\delta + \frac{\omega_{32}}{2}\Big)|3\rangle\langle 3| \\ & - \frac{\hbar\Omega}{2}\Big(|0\rangle\langle 2| + |0\rangle\langle 3| + \text{H.c.}\Big). \end{aligned} \tag{9}$$

Here we define the probe detuning as $\delta = \omega_p - \tilde{\omega}$, where the mean optical transition frequency is $\tilde{\omega} = \frac{1}{2}(\omega_3 + \omega_2) - \omega_0$. The excited-state splitting is $\omega_{32} = \omega_3 - \omega_2$. The probe Rabi frequency is $\Omega = \mu E_p/(\sqrt{2}\hbar)$, with μ the relevant dipole matrix element and E_p the probe-field amplitude. In our configuration the probe addresses the $|0\rangle \leftrightarrow |2\rangle$ and $|0\rangle \leftrightarrow |3\rangle$ transitions simultaneously. The bare energies are $E_n = \hbar\omega_n$ for $n = 0, 1, 2, 3$.

Both excited states $|2\rangle$ and $|3\rangle$ decay radiatively to $|0\rangle$ with rates $2\gamma_2'$ and $2\gamma_3'$, respectively, and to $|1\rangle$ with rates $2\gamma_2$ and $2\gamma_3$. We assume that the $|2\rangle, |3\rangle \rightarrow |1\rangle$ transitions lie within the surface-plasmon bands of the nearby nanostructure, whereas the $|2\rangle, |3\rangle \rightarrow |0\rangle$ transitions are spectrally well outside those bands and therefore experience ordinary free-space spontaneous emission. We work in the regime of a small excited-state splitting and take equal decay parameters for the two excited states, $\gamma_2 = \gamma_3 \equiv \gamma$ and $\gamma_2' = \gamma_3' \equiv \gamma'$. Coupling between $|2\rangle$ and $|3\rangle$ mediated by the modified, anisotropic vacuum is accounted for by a real coefficient κ, which produces spontaneously generated coherence. From the Hamiltonian in Eq. (9) and a Markovian master equation, the density-matrix elements obey

$$\dot{\rho}_{00} = 2\gamma'\big(\rho_{22} + \rho_{33}\big) - \frac{i\Omega}{2}\big(\rho_{02} - \rho_{20}\big) - \frac{i\Omega}{2}\big(\rho_{03} - \rho_{30}\big), \tag{10}$$

$$\dot{\rho}_{22} = -2(\gamma + \gamma')\rho_{22} + \frac{i\Omega}{2}\big(\rho_{02} - \rho_{20}\big) - \kappa\big(\rho_{23} + \rho_{32}\big), \tag{11}$$

$$\dot{\rho}_{33} = -2(\gamma + \gamma')\rho_{33} + \frac{i\Omega}{2}\big(\rho_{03} - \rho_{30}\big) - \kappa\big(\rho_{23} + \rho_{32}\big), \tag{12}$$

$$\dot{\rho}_{20} = \Big(i\delta + i\frac{\omega_{32}}{2} - \gamma - \gamma'\Big)\rho_{20} - \frac{i\Omega}{2}\rho_{22} - \frac{i\Omega}{2}\rho_{23} + \frac{i\Omega}{2}\rho_{00} - \kappa\rho_{30}, \tag{13}$$

$$\dot{\rho}_{30} = \Big(i\delta - i\frac{\omega_{32}}{2} - \gamma - \gamma'\Big)\rho_{30} - \frac{i\Omega}{2}\rho_{33} - \frac{i\Omega}{2}\rho_{32} + \frac{i\Omega}{2}\rho_{00} - \kappa\rho_{20}, \tag{14}$$

$$\dot{\rho}_{23} = \big(i\omega_{32} - 2\gamma - 2\gamma'\big)\rho_{23} + \frac{i\Omega}{2}\rho_{03} - \frac{i\Omega}{2}\rho_{20} - \kappa\big(\rho_{22} + \rho_{33}\big), \tag{15}$$

with the constraints $\rho_{00} + \rho_{11} + \rho_{22} + \rho_{33} = 1$ and $\rho_{mn} = \rho_{nm}^*$. The parameter κ represents the vacuum-induced coupling between $|2\rangle$ and $|3\rangle$ and is responsible for the emergence of quantum-interference effects. In addition, the present treatment does not explicitly include pure dephasing of the optical coherences or inhomogeneous broadening of the emitter transition frequencies. These effects are expected to be especially relevant for realistic solid-state emitter ensembles. Their main influence would be to reduce the coherence underlying the plasmon-induced transparency feature, broaden the spectral response, and weaken the steep dispersive variation of the effective susceptibility.

The spontaneous emission rate γ and the quantum interference κ between the excited states follow from the local electromagnetic Green's tensor $\mathbf{G}(\mathbf{r},\mathbf{r};\bar{\omega})$ as

$$\gamma = \frac{\mu_0\mu^2\bar{\omega}^2}{\hbar}\,\hat{\varepsilon}_-\cdot \operatorname{Im}\mathbf{G}(\mathbf{r},\mathbf{r};\bar{\omega})\cdot\hat{\varepsilon}_+, \tag{16}$$

$$\kappa = \frac{\mu_0\mu^2\bar{\omega}^2}{\hbar}\,\hat{\varepsilon}_+\cdot \operatorname{Im}\mathbf{G}(\mathbf{r},\mathbf{r};\bar{\omega})\cdot\hat{\varepsilon}_+. \tag{17}$$

Here, $\mathbf{r}$ locates the emitter, μ_0 is the vacuum permeability, and $\bar{\omega} = (\omega_3+\omega_2)/2 - \omega_1$. Using the tensor components normal ($\perp$) and parallel ($\|$) to the nearby surface, we write

$$\gamma = \frac{\mu_0\mu^2\bar{\omega}^2}{2\hbar}\operatorname{Im}\left[G_\perp(\mathbf{r},\mathbf{r};\bar{\omega}) + G_\|(\mathbf{r},\mathbf{r};\bar{\omega})\right] = \frac{1}{2}\left(\Gamma_\perp + \Gamma_\|\right), \tag{18}$$

$$\kappa = \frac{\mu_0\mu^2\bar{\omega}^2}{2\hbar}\operatorname{Im}\left[G_\perp(\mathbf{r},\mathbf{r};\bar{\omega}) - G_\|(\mathbf{r},\mathbf{r};\bar{\omega})\right] = \frac{1}{2}\left(\Gamma_\perp - \Gamma_\|\right). \tag{19}$$

We use $G_\perp(\mathbf{r},\mathbf{r};\bar{\omega}) = G_{zz}(\mathbf{r},\mathbf{r};\bar{\omega})$ and $G_\|(\mathbf{r},\mathbf{r};\bar{\omega}) = G_{xx}(\mathbf{r},\mathbf{r};\bar{\omega})$. The rates $\Gamma_\perp$ and $\Gamma_\|$ correspond to dipole orientations normal (along z) and parallel (along x) to the surface, with $\Gamma_{\perp,\|} = \mu_0\mu^2\bar{\omega}^2\operatorname{Im}[G_{\perp,\|}]/\hbar$. The interference degree is $p = (\Gamma_\perp - \Gamma_\|)/(\Gamma_\perp + \Gamma_\|)$. In vacuum one has $\Gamma_\perp = \Gamma_\|$ and hence $\kappa = 0$.

We consider a 2D square array of electromagnetic scatterers [Fig. 1(d)]. The relevant electric–electric Green's tensor component at the emitter location can be written as

$$\begin{aligned} G_{ii}^{EE}(\mathbf{r},\mathbf{r};\omega) = g_{ii}^{EE}(\mathbf{r},\mathbf{r};\omega) &- \frac{i}{8\pi^2}\int_{\mathrm{SBZ}} d^2\mathbf{k}_\| \sum_{\mathbf{g}} \frac{1}{c^2 K_{\mathbf{g},z}^+} \\ &\times \mathbf{v}_{\mathbf{g},\mathbf{k}_\|;i}(\mathbf{r})\,\exp\left[-i\mathbf{K}_{\mathbf{g}}^+\cdot\mathbf{r}\right]\hat{\mathbf{e}}_i(\mathbf{K}_{\mathbf{g}}^+), \end{aligned} \tag{20}$$

with

$$\mathbf{v}_{\mathbf{g},\mathbf{k}_\|;i}(\mathbf{r}) = \sum_{\mathbf{g}'} R_{\mathbf{g};\mathbf{g}'}(\omega,\mathbf{k}_\|)\exp\left[-i\mathbf{K}_{\mathbf{g}'}^-\cdot\mathbf{r}\right]\hat{\mathbf{e}}_i(\mathbf{K}_{\mathbf{g}'}^-), \tag{21}$$

and reduced wavevectors

$$\mathbf{K}_{\mathbf{g}}^\pm = \{\mathbf{k}_\| + \mathbf{g},\ \pm[k_0^2 - |\mathbf{k}_\| + \mathbf{g}|^2]^{1/2}\}, \qquad k_0 = \omega/c. \tag{22}$$

Here, $\mathbf{g}$ are reciprocal lattice vectors of the 2D array, SBZ is the surface Brillouin zone, g_{ii}^{EE} is the free-space Green's tensor, $\hat{\mathbf{e}}_i(\cdot)$ are unit polarization vectors, and $R_{\mathbf{g};\mathbf{g}'}$ is the reflection matrix that sums all diffracted orders.

The plasmonic nanostructure used throughout this work is the same periodic nanoshell platform analyzed in our earlier studies on transparency, absorption control, and spatially structured emission in emitter–plasmon hybrids [8,10,14]. More specifically, we consider a two-dimensional square lattice of silica nanospheres coated by a metallic shell. The dielectric core has permittivity $\epsilon = 2.1$ and radius $S_c = 0.7\,c/\omega_p$, the outer sphere radius is $S = c/\omega_p$, and the lattice constant is $a = 2\,c/\omega_p$. The metal shell is modeled by the Drude permittivity

$$\varepsilon(\omega) = 1 - \frac{\omega_p^2}{\omega(\omega + i/\tau)}, \tag{23}$$

with $\hbar\omega_p = 8.99$ eV and $\tau^{-1} = 0.05\,\omega_p$, so that the characteristic length scale is $c/\omega_p \simeq 22$ nm. The parameter set adopted here also suggests a plausible route toward experimental implementation. Using the characteristic scale $c/\omega_p \simeq 22$ nm, the modeled structure corresponds to silica-core/metal-shell nanoparticles with core radius $S_c \approx 15.4$ nm, outer radius $S \approx 22$ nm, and lattice constant $a \approx 44$ nm, arranged in a periodic nanoshell array. A possible realization would therefore consist of fabricating such a nanostructured plasmonic layer, introducing a thin emitter-host or spacer layer to control the emitter–metal separation d, and embedding this active region within the planar cavity used in the transfer-matrix description. In practice, the most direct experimental control parameters would be the nanoshell geometry and array period, the emitter–surface distance, the cavity thickness, and the probe incidence angle, detuning, and intensity. The predicted PSHE could then be investigated in reflection by resolving the opposite spin components of the reflected beam, either through direct beam-centroid tracking or through weak-measurement amplification in the resonant angular interval where the displacement is strongest. The present discussion is intended to indicate a plausible experimental route rather than to provide a fabrication-specific optimization of the device.

At the level of the present model, intrinsic metallic loss is included phenomenologically through the finite damping rate in the Drude permittivity of Eq. (23). This loss enters the reflection matrix and the Green-tensor calculation, and therefore influences the plasmon-modified decay rates, the effective susceptibility, and the resulting cavity reflection response. By contrast, extrinsic loss mechanisms such as surface roughness, fabrication-induced disorder, and additional diffuse scattering are not treated explicitly here. The present calculations should therefore be interpreted as describing an idealized periodic structure with intrinsic Ohmic damping included, but without a full device-level treatment of structural imperfections.

The modified spontaneous-emission rates $\Gamma_\perp$ and $\Gamma_\|$ entering the density-matrix model are obtained from the perpendicular and parallel components of the electromagnetic Green tensor of the periodic nanoshell array, evaluated at the emitter position, following the multiple-scattering/Green-tensor formalism presented above. In practice, the reflection matrix of the periodic structure is first computed and then inserted into the Green-tensor expression to extract the plasmon-modified local density of optical states and the corresponding decay channels. The same calculation also yields the distance-dependent interference parameter p. Over the distances of interest the parallel rate $\Gamma_\|$ is strongly suppressed relative to free space, while $\Gamma_\perp$ can be enhanced near the array. Consequently $p \gtrsim 0.95$ and often > 0.99. For the three representative separations used in the main text, we obtain $\Gamma_\perp = 8.080\,\Gamma_0$ and $\Gamma_\| = 0.015\,\Gamma_0$ for $d = 0.3\,c/\omega_p$, $\Gamma_\perp = 1.237\,\Gamma_0$ and $\Gamma_\| = 0.0044\,\Gamma_0$ for $d = 0.6\,c/\omega_p$, and $\Gamma_\perp = 0.439\,\Gamma_0$ and $\Gamma_\| = 0.002\,\Gamma_0$ for $d = 0.8\,c/\omega_p$.

For a weak probe field, the linear (first-order) optical susceptibility of the quantum-emitter layer is defined as

$$\chi^{(1)}(\delta) = \frac{N\mu^2}{\varepsilon_0\hbar\,\Omega}\left(\rho_{20}^{(1)} + \rho_{30}^{(1)}\right), \tag{24}$$

where $\Omega = \mu E_p/(\sqrt{2}\hbar)$ is the probe Rabi frequency and N is the emitter density. Solving Eqs. (10)–(15) to first order in the probe field gives

$$\rho_{20}^{(1)} = \frac{\frac{i\Omega}{2}\left(-i\delta + \frac{i\omega_{32}}{2} + \gamma + \gamma'\right) - \frac{i\kappa\Omega}{2}}{\left(-i\delta + \frac{i\omega_{32}}{2} + \gamma + \gamma'\right)\left(-i\delta - \frac{i\omega_{32}}{2} + \gamma + \gamma'\right) - \kappa^2}, \tag{25}$$

$$\rho_{30}^{(1)} = \frac{\frac{i\Omega}{2}\left(-i\delta - \frac{i\omega_{32}}{2} + \gamma + \gamma'\right) - \frac{i\kappa\Omega}{2}}{\left(-i\delta + \frac{i\omega_{32}}{2} + \gamma + \gamma'\right)\left(-i\delta - \frac{i\omega_{32}}{2} + \gamma + \gamma'\right) - \kappa^2}. \tag{26}$$

Substituting Eqs. (25) and (26) into Eq. (24) and using Eqs. (18) and (19) yields, after some algebra,

$$\chi^{(1)}(\delta) = \frac{N\mu^2}{\varepsilon_0\hbar}\,\frac{\delta + i\gamma' + i\Gamma_\|}{-\delta^2 + \frac{\omega_{32}^2}{4} + (\Gamma_\perp + \gamma')(\Gamma_\| + \gamma') - i\delta\left(\Gamma_\perp + \Gamma_\| + 2\gamma'\right)}. \tag{27}$$

Eq. (27) fully characterizes the linear optical response of the active quantum-emitter layer and constitutes the susceptibility that enters the cavity model in the strictly weak-field regime.

The third-order susceptibility originates from the cubic-order coherences $\rho_{20}^{(3)}$ and $\rho_{30}^{(3)}$, obtained by solving Eqs. (10)–(15) perturbatively up to order Ω^3. In direct analogy with Eq. (24), the third-order susceptibility is expressed as

$$\chi^{(3)}(\delta) = \frac{N\mu^2}{\varepsilon_0 \hbar\, \Omega^3}\left(\rho_{20}^{(3)} + \rho_{30}^{(3)}\right), \tag{28}$$

which gives $\chi^{(3)}(\delta) = \frac{N\mu^4}{\varepsilon_0 \hbar^3} F(\delta)$, where the dimensionless spectral function $F(\delta)$ is

$$F(\delta) = \frac{(\delta + i\gamma' + i\Gamma_{\|})\left[(\delta + i\gamma' + i\Gamma_{\|})^2 - \frac{\omega_{32}^2}{4} - \kappa^2\right]}{\left[-\delta^2 + \frac{\omega_{32}^2}{4} + (\Gamma_{\perp} + \gamma')(\Gamma_{\|} + \gamma') - i\delta(\Gamma_{\perp} + \Gamma_{\|} + 2\gamma')\right]^3}. \tag{29}$$

This expression possesses the same complex poles as the linear susceptibility of Eq. (27), while incorporating higher-order saturation and coherence-redistribution effects characteristic of Kerr-type nonlinearities. The form of $F(\delta)$ is fully consistent with the perturbative solution and ensures that the nonlinear correction preserves the spectral structure dictated by the underlying quantum-emitter dynamics.

The intracavity permittivity $\epsilon_2 = 1 + \chi_{\text{eff}}$ defined in Section 2.1 depends on the effective susceptibility of the emitter layer. In the weak-probe limit the effective susceptibility reduces to the linear response, $\chi_{\text{eff}} \to \chi^{(1)}$.

To account for optical-intensity effects beyond the linear regime, we incorporate the leading nonlinear correction arising from the Kerr-type third-order response of the emitters. Within the standard perturbative expansion in the probe-field amplitude, the effective susceptibility is written as

$$\chi_{\text{eff}}(\delta) = \chi^{(1)}(\delta) + \tfrac{3}{4}\,\chi^{(3)}(\delta)\,|\Omega|^2. \tag{30}$$

The numerical factor 3/4 follows from the harmonic-field expansion employed in the perturbative treatment of the density-matrix equations.

The perturbative expansion implicit in Eq. (30) is controlled by the probe-field strength through $|\Omega|$. It is quantitatively reliable only in the weak-excitation regime, where the cubic correction remains the leading nonlinear contribution and the resulting χ_{eff} stays close to the full steady-state susceptibility. As the driving field increases, higher-order saturation and coherence-redistribution effects become progressively more important, and low-order perturbative truncations no longer provide a quantitatively reliable description of the nonlinear response. In that regime, the all-orders steady-state solution of the density-matrix equations should be regarded as the appropriate reference.

Since the probe Rabi frequency scales as $\Omega \propto E_p$, the nonlinear contribution in Eq. (30) introduces an intensity-dependent correction to both the absorptive and dispersive parts of the susceptibility. This correction modifies the intracavity permittivity and, through the reflection coefficients $R_{s,p}$, directly affects the spin-dependent transverse displacement described by Eq. (5). In this way, the optical intensity provides an additional coherent control parameter, complementary to the probe detuning δ, the incidence angle θ_i, and the emitter–metal separation d.

Within this framework, the formulation naturally supports different levels of theoretical description, depending on the extent to which nonlinear effects are included. In the analysis that follows, we distinguish three representative levels: (i) the first-order susceptibility $\chi^{(1)}$, corresponding to the strictly linear response, (ii) the perturbative effective susceptibility χ_{eff} defined in Eq. (30), which includes the leading third-order correction, and (iii) the all-orders susceptibility obtained from the full steady-state solution of the density-matrix equations without perturbative truncation in Ω. This hierarchy provides a systematic and physically transparent framework for evaluating how nonlinear optical effects influence the predicted PSHE response.

Finally, we emphasize that the present formulation is intended to isolate the underlying mechanism of PSHE control in a hybrid emitter–plasmonic cavity under idealized conditions. The model assumes a perfectly periodic nanoshell array, a homogeneous emitter layer, and a Markovian description of the emitter dynamics. It does not explicitly include fabrication-induced disorder, particle-size dispersion, surface roughness, emitter-position uncertainty, pure dephasing, inhomogeneous broadening, or additional nonradiative quenching channels. Accordingly, the calculated spin Hall shifts should be interpreted as proof-of-principle theoretical predictions and trend estimates, rather than as quantitative device-performance bounds. Incorporating such realistic effects, together with experimental validation, is an important direction for future work.

3. Results and discussion

3.1. Distance-dependent plasmonic hybridization in the linear regime

We begin by establishing a baseline in the absence of any plasmonic element. Fig. 2(a) displays the complex linear probe susceptibility for a homogeneous quantum medium. The absorptive component Im[χ] (purple solid curve) exhibits a single resonance centered at $\delta \approx 0$, without any transparency window or steep dispersive enhancement. The dispersive component Re[χ] (orange dashed curve) is odd-symmetric, crossing zero at resonance and changing sign across $\delta = 0$, consistent with Kramers-Kronig causality. This spectrum represents the intrinsic linear optical response of the emitters in the absence of any modification to the local electromagnetic density of states by metallic nanostructures.

Having established the reference susceptibility, we next examine the polarization-resolved reflection response at resonance. In Fig. 2(b), setting $\delta = 0$, we plot the magnitudes of the total multilayer reflection coefficients $|R_s|$ (TE) and $|R_p|$ (TM), obtained from Eq. (1), as functions of the incidence angle θ_i. At normal incidence the two coefficients coincide, $|R_p| \approx |R_s|$, as required by symmetry, since the TE and TM boundary conditions become identical. As θ_i increases, $|R_p|$ decreases and develops a shallow, broad minimum at an intermediate angle. This minimum does not correspond to a Brewster zero of a single interface, but arises from interference between the two cavity interfaces encoded in Eq. (1). In contrast, $|R_s|$ varies smoothly and increases monotonically with θ_i. For larger θ_i, both $|R_p|$ and $|R_s|$ increase toward large values, consistent with the enhanced reflectivity of the multilayer at oblique incidence. The resulting polarization asymmetry is an intrinsic property of multilayer interference rather than a single-interface effect, and it provides one of the two key control parameters entering the PSHE expression in Eq. (5).

Building on this analysis, Fig. 2(c) quantifies the polarization-channel imbalance at $\delta = 0$ through the ratio $|R_s|/|R_p|$. The ratio exhibits a moderate maximum at the same incidence angle where $|R_p|$ reaches its minimum. This enhancement originates from the interference-induced suppression of the TM reflection coefficient within the multilayer cavity, while $|R_s|$ remains finite and varies smoothly across this angular range. Outside this angular interval, $|R_p|$ increases and approaches $|R_s|$, causing the ratio to decrease toward values close to unity. The peak in Fig. 2(c) therefore marks the angular region of maximal polarization contrast. However, as made explicit by Eq. (5), the PSHE is not governed solely by the amplitude ratio $|R_s|/|R_p|$, but by its interplay with the angular derivative of the complex TM reflection coefficient [see Eq. (6)]. In physical terms, this means that the TE and TM channels contribute unequally to the reflected beam in this angular range, thereby creating the polarization asymmetry required for pronounced spin-dependent splitting. Near resonance, this angular derivative receives contributions from both the variation of $|R_p|$ and the angular phase gradient $\partial_{\theta_i} \arg(R_p)$. Consequently, the reflection minimum identifies the sign-transition region, whereas the PSHE extrema generally occur at nearby angles where the combined amplitude-phase contribution is maximized. This mechanism will be used below as the common framework for interpreting the distance- and nonlinearity-dependent results.

Finally, Fig. 2(d) presents the transverse photonic spin Hall (Imbert-Fedorov) shift δ_{p+}/λ as a function of θ_i at $\delta = 0$. For small incidence angles, the shift is positive and relatively weak, then increases to a

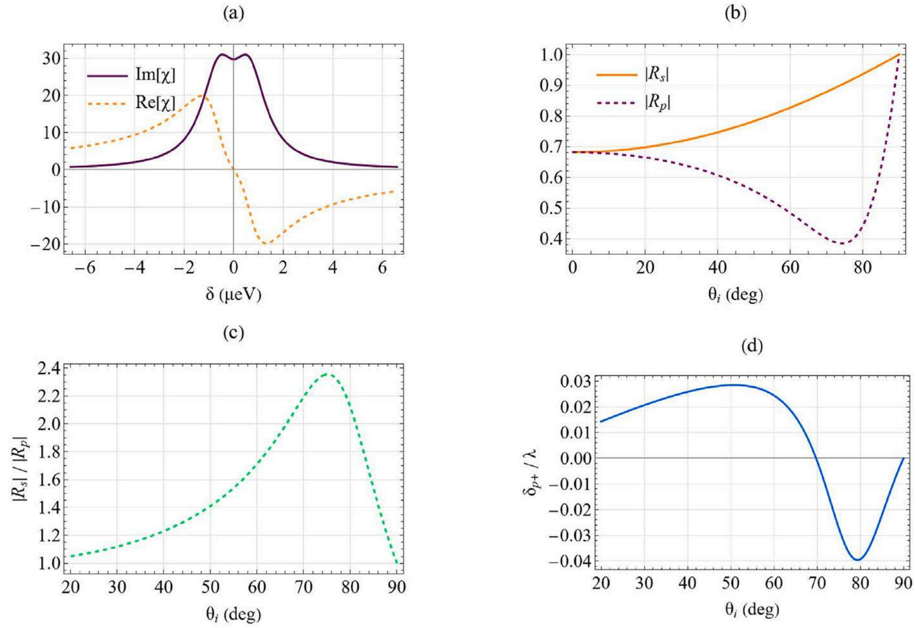

Fig. 2. (a) Imaginary part, Im$[\chi]$ (purple solid curve), and real part, Re$[\chi]$ (orange dashed curve), of the linear probe susceptibility as functions of the probe detuning δ. (b) Magnitudes of the reflection coefficients $|R_p|$ (orange solid curve) and $|R_s|$ (purple dashed curve), plotted versus the incidence angle θ_i at $\delta = 0$. (c) Reflection-channel imbalance quantified by $|R_s|/|R_p|$ as a function of θ_i at $\delta = 0$. (d) Photonic spin Hall (Imbert-Fedorov) shift δ_{p+}/λ versus θ_i at $\delta = 0$. Panels (a)-(d) correspond to the configuration without a plasmonic nanostructure. Unless stated otherwise, parameters are $\omega_{32} = 1.5\,\Gamma_0$, $\gamma' = 0$, $\Gamma_\perp = \Gamma_0$, $\Gamma_\parallel = \Gamma_0$, $\mathcal{N} = 10^{12}\,\mathrm{m}^{-3}$, $\mu_{03} = 3.79 \times 10^{-29}\,\mathrm{C\,m}$, $\epsilon_1 = \epsilon_3 = 2.22$, Gaussian beam with waist $\omega_0 = 50\lambda$, $\lambda = 692\,\mathrm{nm}$, and intracavity thickness $q = 100\,\mathrm{nm}$, where Γ_0 denotes the free-space spontaneous emission rate.

moderate maximum. As θ_i is further increased, δ_{p+} crosses zero, reverses sign, and reaches a comparatively shallow negative minimum before gradually tending back toward zero. The sign reversal reflects the inversion of the spin-dependent transverse beam displacement upon reflection. The angular positions of the extrema do not coincide with the minimum of $|R_p|$. As follows from Eq. (5), the shift is governed jointly by the amplitude-related factor $|R_s|/|R_p|$ and by the angular dispersion of R_p through $\partial_{\theta_i} \ln R_p$. Importantly, the negative shift minimum occurs at a significantly larger incidence angle than the amplitude minimum of $|R_p|$ and the corresponding imbalance maximum. This angular offset directly demonstrates that the PSHE is not governed solely by reflection-amplitude suppression, but is critically controlled by the angular phase dispersion of R_p. Thus, the TM reflection minimum identifies the vicinity of the sign-transition region, while the extrema appear slightly away from it, where the polarization imbalance remains strong and the phase-gradient contribution is still sufficiently large to enhance the displacement. This observation provides clear evidence that phase-gradient enhancement constitutes a distinct and essential mechanism for spin–orbit interaction, even in the absence of plasmonic coupling.

This analysis demonstrates that, even in the absence of plasmonic coupling, the PSHE can be tuned through angular control of the multilayer reflection response governed by Eq. (1). We now proceed to introduce a plasmonic nanostructure, where the emitter-SPP interaction reshapes $\chi(\delta)$, modifies the p-polarized reflection profile, and enhances both the amplitude imbalance and the angular phase dispersion, leading to strongly amplified and sign-reversible spin Hall shifts.

The physical mechanism is therefore the following: plasmonic hybridization first reshapes the complex susceptibility through PIT-like interference, this modified susceptibility then alters the TE/TM reflection asymmetry and the angular phase response of the TM channel, and these two quantities together determine the magnitude, sign, and angular position of the PSHE extrema.

We now introduce the plasmonic interface and position the emitter layer at a subwavelength distance $d = 0.3c/\omega_p$ from the metal surface. Fig. 3 summarizes how this near-field hybridization reshapes the emitter susceptibility, the polarization-resolved cavity reflection, and the resulting photonic spin Hall shift.

In Fig. 3(a), the absorptive component Im$[\chi]$ no longer exhibits the single-peaked Lorentzian profile of Fig. 2(a). Instead, it develops a narrow suppression centered at $\delta \approx 0$, embedded within a broader absorptive background, while Re$[\chi]$ acquires a markedly steeper odd-symmetric variation across resonance. Within a narrow detuning interval, absorption is strongly reduced and the spectral derivative of Re$[\chi]$ is enhanced. By causality, this suppression of absorption is necessarily accompanied by increased dispersive variation, reflecting the Kramers-Kronig relation. The combined response constitutes the characteristic signature of plasmon-induced transparency (PIT), arising from coherent interference between the direct radiative response of the emitters and the surface-plasmon-polariton channel.

At $\delta = 0$, Fig. 3(b) shows that $|R_p|$ develops a substantially deeper minimum than in Fig. 2(b), while $|R_s|$ remains smooth and monotonic. Since only the TM polarization efficiently couples to SPP modes, the plasmonic interface predominantly modifies the p channel. Compared with the baseline, the p-channel minimum is both deeper and shifted in angle, indicating modified interference conditions within the hybrid cavity defined by Eq. (1). As a result, the imbalance $|R_s|/|R_p|$ in Fig. 3(c) increases, with the peak value clearly exceeding that of Fig. 2(c). This enhancement originates from the strong suppression of $|R_p|$ rather than from any substantial growth of $|R_s|$. Relative to the no-nanostructure case, the hybrid configuration therefore generates a moderately stronger reflection-channel imbalance in the angular region relevant for spin–orbit conversion. As in Fig. 2, this angular position lies close to a zero crossing of δ_{p+}, indicating that the plasmon-induced reflection minimum marks the angular region associated with the transition between opposite spin Hall displacement directions.

The impact on the PSHE is shown in Fig. 3(d). The angular dependence becomes sharper and the extrema increase substantially in magnitude compared with Fig. 2(d). The curve exhibits a positive

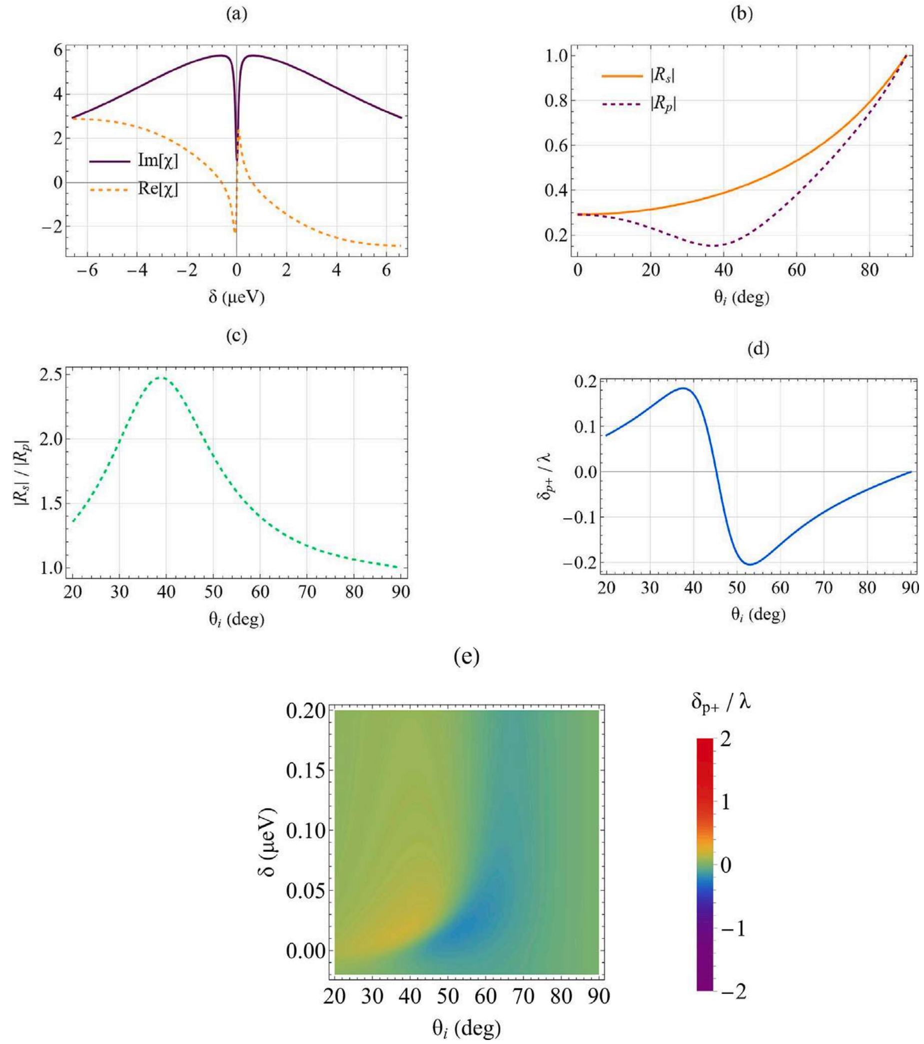

Fig. 3. (a) Imaginary part, Im[χ] (purple solid curve), and real part, Re[χ] (orange dashed curve), of the linear probe susceptibility as functions of δ. (b) Magnitudes of the reflection coefficients $|R_p|$ (orange solid) and $|R_s|$ (purple dashed), plotted versus θ_i at $\delta = 0$. (c) Reflection-channel imbalance $|R_s|/|R_p|$ versus θ_i at $\delta = 0$. (d) PSHE shift δ_{p+}/λ versus θ_i at $\delta = 0$. (e) Density map of δ_{p+}/λ as a function of (θ_i, δ). Panels correspond to the configuration with a plasmonic nanostructure, with emitter–metal separation $d = 0.3\,c/\omega_p$ giving $\Gamma_\perp = 8.080\,\Gamma_0$ and $\Gamma_\parallel = 0.015\,\Gamma_0$. The other parameters are the same as in Fig. 2.

maximum followed by a sign reversal and a negative minimum within a narrow angular interval. The reflection minimum and imbalance peak occur close to the zero crossing of δ_{p+}, marking the transition between opposite displacement directions. This behavior is consistent with the general mechanism introduced above. Relative to Fig. 2, the main effect here is that plasmonic hybridization sharpens the angular response and increases the PSHE magnitude.

Fig. 3(e) presents the two-dimensional map of δ_{p+}/λ in the (θ_i, δ) plane. A narrow sign-switching ridge separates regions of opposite displacement polarity, demonstrating controlled switching of the PSHE sign through small adjustments of incidence angle or detuning. The ridge intersects the angular axis in the same resonant angular region where the reflection minimum occurs, indicating that the reflection minimum is closely associated with the sign-transition boundary of the spin Hall shift. In this configuration, both control terms entering Eq. (5) are simultaneously enhanced and the system operates in a balanced hybrid regime where amplitude contrast and phase dispersion reinforce each other.

We next examine the case $d = 0.6c/\omega_p$ (Fig. 4), where the emitter–metal separation is increased relative to Fig. 3 and the hybrid response is correspondingly modified. This increase in separation does not simply strengthen the previous behavior. Instead, it shifts the system into a distinct hybrid regime in which the relative balance between amplitude contrast and phase dispersion is altered.

In Fig. 4(a), the PIT signature persists: Im[χ] still exhibits a narrow suppression of absorption around $\delta \approx 0$, while Re[χ] retains a steep odd-symmetric dispersion. However, compared directly with Fig. 3(a), the transparency dip is not visibly shallower. Instead, it remains very deep, while the transparency feature becomes more spectrally localized at this larger separation. The transparency window remains clearly identifiable, but its spectral contrast is reduced compared with the smaller-separation case.

At $\delta = 0$, Fig. 4(b) shows that $|R_p|$ again develops a pronounced minimum at an intermediate incidence angle, while $|R_s|$ varies smoothly and increases monotonically. The p-channel minimum is significantly deeper than in Fig. 3(b), confirming that the interference induced by the quantum-plasmonic hybrid structure produces stronger suppression of the TM reflection channel at this separation. The corresponding imbalance $|R_s|/|R_p|$ in Fig. 4(c) remains strongly peaked near the same angular region, with a maximum value significantly higher than in Fig. 3(c). As before, this angular position lies in the same resonant angular region as a zero crossing of δ_{p+} in Fig. 4(d). Outside this angular

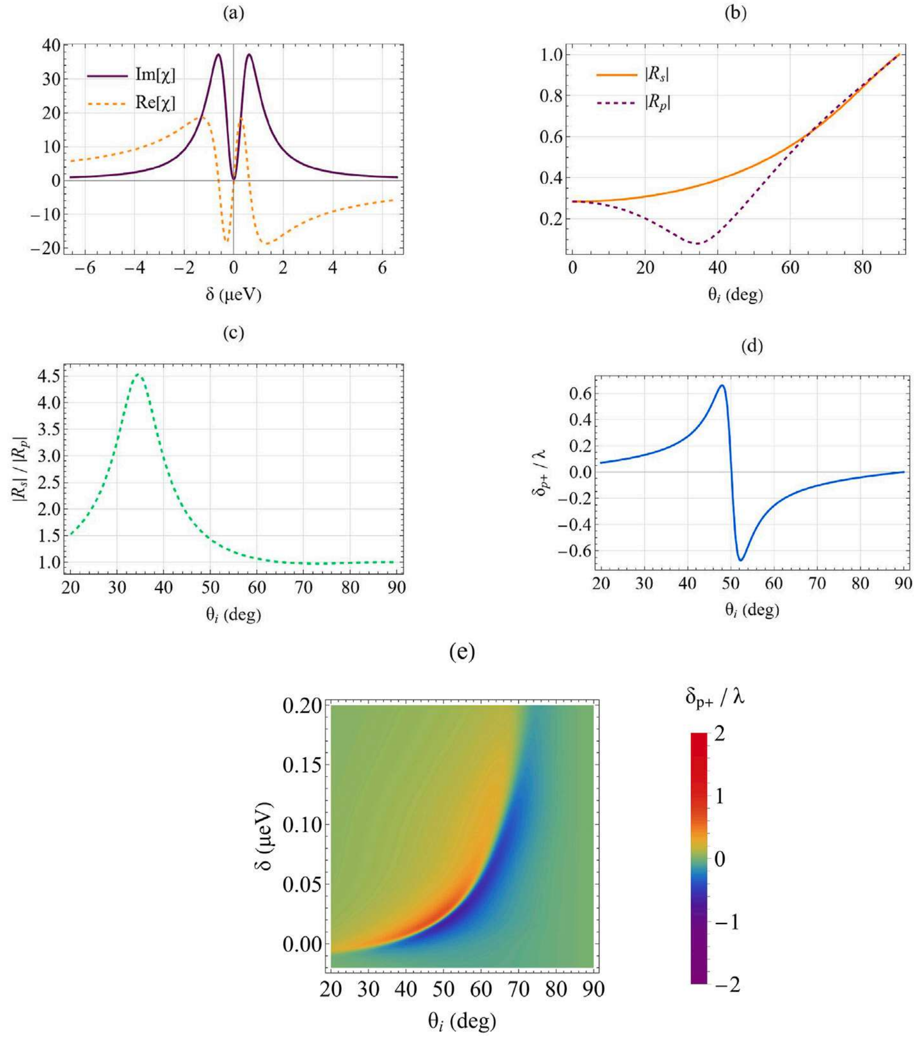

Fig. 4. Same as Fig. 3 but for emitter–metal separation $d = 0.6\,c/\omega_p$ giving $\Gamma_\perp = 1.237\,\Gamma_0$ and $\Gamma_\parallel = 0.0044\,\Gamma_0$. The other parameters are the same as in Fig. 2.

interval, $|R_p|$ increases and approaches $|R_s|$, reducing the polarization contrast toward unity. The amplitude-based contribution to the PSHE is therefore significantly enhanced compared with the $d = 0.3c/\omega_p$ case. At the same time, Fig. 4(a) indicates that this enhancement is not accompanied by a uniformly stronger PIT signature than in Fig. 3(a). Rather, the transparency feature remains clearly identifiable but becomes more spectrally localized, while the angular reflection imbalance and the PSHE response appear to be enhanced more strongly than the transparency dip itself.

Despite this increase in amplitude contrast, Fig. 4(d) shows that the PSHE response becomes more strongly amplified and more localized in angle than in Fig. 3. The underlying mechanism remains the same. However, this behavior should not be interpreted as a simple uniform strengthening of the hybrid response. Instead, it is consistent with a more favorable balance between reflection-channel imbalance and angular phase dispersion within the same resonant angular region.

Moreover, the density map in Fig. 4(e) displays a thin sign-switching boundary separating regions of opposite displacement. Compared with Fig. 3(e), the ridge exhibits stronger contrast and larger displacement magnitude, confirming enhanced spin–orbit control at this separation.

In Fig. 5, we consider the configuration with $d = 0.8c/\omega_p$, which completes the progression established in Figs. 3 and Fig. 4. Over the separations considered here ($d = 0.3\text{-}0.8\,c/\omega_p$), largest PSHE extrema shown in Figs. 3–5 increase overall, but the response remains governed by two distance-dependent contributions entering Eq. (5): the suppression of the p-polarized reflection amplitude and the angular phase dispersion of the same channel.

In Fig. 5(a), the transparency-like structure in the susceptibility remains clearly visible but becomes more spectrally localized and narrower compared with Figs. 3 and 4, indicating that the hybrid interference persists while being confined to a smaller detuning interval. At resonance, Fig. 5(b) shows that $|R_p|$ is suppressed to a very small value near an intermediate incidence angle, while $|R_s|$ remains smooth and comparatively large. This represents the deepest reflection minimum among all separations considered. The system therefore approaches a near-zero-reflection regime for the p-polarized channel that is qualitatively distinct from the smaller-separation configurations.

As a direct consequence, the polarization-channel imbalance in Fig. 5(c) increases dramatically, reaching values approximately 3.5 times larger than in Fig. 3 and about twice as large as in Fig. 4. Consistent with the previous cases, this angular position appears near a zero crossing of δ_{p+} in Fig. 5(d). This enhancement originates primarily from the near-vanishing of $|R_p|$ within a narrow angular interval rather than from any substantial growth of $|R_s|$. Simultaneously, the angular phase of R_p varies extremely rapidly in the same angular region. The angular phase dispersion, governed by $\partial_{\theta_i} \ln R_p$, becomes extremely steep near the reflection minimum.

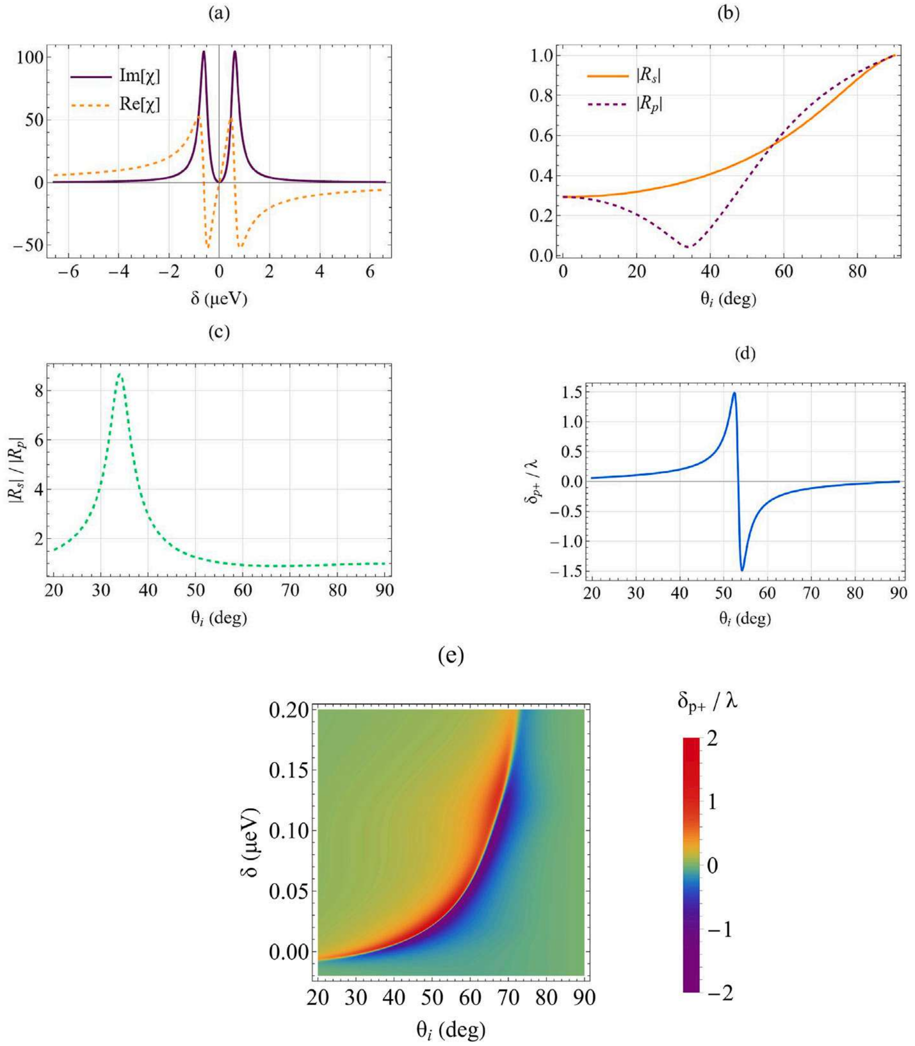

Fig. 5. Same as Fig. 3 but for emitter–metal separation $d = 0.8\,c/\omega_p$ giving $\Gamma_\perp = 0.439\,\Gamma_0$ and $\Gamma_\parallel = 0.002\,\Gamma_0$. The other parameters are the same as in Fig. 2.

In Fig. 5(d), the normalized displacement δ_p^+/λ exhibits the largest extrema among the separations considered. What distinguishes this case is the approach to a near-zero-$|R_p|$ regime, where Eq. (5) predicts a strongly amplified and sharply localized spin Hall response due to the combined enhancement of the reflection-channel imbalance and the angular response of the complex TM reflection coefficient. This regime, however, must be interpreted with care from an experimental standpoint. Because the same condition is accompanied by a strong suppression of the reflected p-polarized intensity, the largest normalized shifts do not necessarily correspond to the most favorable operating point for observation. In practice, finite beam divergence, angular averaging over the incident beam profile, alignment imperfections, detector noise, and finite measurement sensitivity are expected to smooth the sharpest features and reduce the effectively measured displacement. The largest values shown here should therefore be interpreted as idealized upper-bound predictions of the model.

The two-dimensional map in Fig. 5(e) further highlights the strongly localized angular-detuning structure. Compared with Figs. 3(e) and 4(e), the ridge becomes significantly sharper and exhibits much higher contrast, indicating the extreme sensitivity of the PSHE to the angular phase response near the reflection minimum. From a practical standpoint, more robust observation is expected slightly away from the exact near-zero-reflection point, where the displacement remains substantial while the reflected intensity and the corresponding signal-to-noise ratio are more favorable.

Taken together, Figs. 3-5 show a systematic evolution with emitter–metal separation: at $d = 0.3c/\omega_p$ the plasmonic interface sharpens the PSHE response, at $d = 0.6c/\omega_p$ the displacement extrema become larger, and at $d = 0.8c/\omega_p$ the system approaches a near-zero-$|R_p|$ regime with strongly enhanced normalized displacement. This progression should not be viewed as a strictly monotonic strengthening of the response with increasing d. Rather, the response remains governed throughout by the distance-dependent interplay between reflection-amplitude suppression and angular phase dispersion, whose relative balance changes from one separation to another.

It is worth noting that the sharp PIT and PSHE features discussed here are sensitive to plasmonic loss. In general, stronger intrinsic or extrinsic loss is expected to broaden the transparency-like spectral feature, reduce its contrast, and weaken the steep dispersive variation associated with the plasmon-emitter hybrid response. In the angular domain, this would smooth the phase variation of R_p, reduce the depth of the reflection minimum, and weaken the polarization-channel imbalance $|R_s|/|R_p|$. Consequently, both the visibility of the PIT response and the magnitude and sharpness of the predicted PSHE extrema, especially in the near-zero-reflection regime, are expected to decrease under more strongly lossy or disordered experimental conditions.

A full quantitative analysis of the dependence of PIT visibility and PSHE magnitude on the metallic damping parameter is beyond the scope of the present work. Nevertheless, the qualitative trends described above follow directly from the loss-sensitive narrowing and phase-dispersion mechanisms of the hybrid plasmonic response.

3.2. Nonlinear control of the PSHE

The results presented above were obtained in the strictly linear optical regime. We now examine how finite optical intensity modifies the PSHE through the nonlinear effective susceptibility χ_{eff} introduced in Eq. (30). In what follows, we distinguish explicitly between a weak-driving regime, where the perturbative third-order susceptibility remains a useful approximation to the full nonlinear response, and a stronger-driving regime, where comparison with the all-orders solution reveals the quantitative breakdown of low-order perturbative descriptions. Because the reflection coefficients R_s and R_p depend on χ_{eff} through ϵ_2, nonlinear corrections modify both the reflection-channel imbalance and the angular phase dispersion that govern the transverse displacement. To isolate genuine nonlinear phase-dispersion effects from trivial amplitude scaling, the probe Rabi frequency Ω was selected separately for each separation such that the perturbative χ_{eff} closely reproduces the all-orders susceptibility. Under this calibration, the first-order susceptibility exhibits small but finite deviations in both amplitude and dispersive slope. In addition, the probe detuning used in panels (b) and (c) was chosen to maximize the angular deviation of the zero-crossing position of δ_{p+} between the first-order and third-order models, so that the plotted curves correspond to the operating point of maximal nonlinear sensitivity.

Figs. 6-8 examine how these nonlinear corrections influence the PSHE for three representative emitter–metal separations. At $d = 0.3c/\omega_p$, shown in Fig. 6, the first-order and third-order susceptibilities exhibit nearly identical resonance positions and overall spectral structure, differing only slightly in amplitude and dispersive slope near resonance [Fig. 6(a)]. These small spectral differences nevertheless produce a clear shift in the angular phase-matching condition governing the PSHE. The reflection-channel imbalance in Fig. 6(b) reaches its maximum at different angles for the first-order and third-order susceptibilities, demonstrating a pronounced nonlinear shift of the reflection minimum. Consistently, the PSHE displacement in Fig. 6(c) undergoes its sign transition at correspondingly different angles. Importantly, while the angular position of the sign transition shifts significantly, the extrema of the transverse displacement remain nearly unchanged in magnitude, but occur at correspondingly shifted angular positions. This behavior demonstrates that, in the weak-hybridization regime, nonlinear susceptibility corrections primarily shift the angular phase condition governing the sign transition rather than altering the overall magnitude of the PSHE. At $d = 0.6c/\omega_p$, results presented in Fig. 7, the nonlinear influence becomes significantly more pronounced. Although the resonance positions remain unchanged [Fig. 7(a)], the first-order susceptibility exhibits a visibly steeper dispersive slope and larger amplitude than the third-order approximation in the detuning region relevant for the PSHE. These spectral differences produce clear modifications in the reflection imbalance [Fig. 7(b)], shifting the angular position of the reflection minimum and altering the polarization-channel contrast. The transverse shift reaches values on the order of $\pm 0.6\lambda$, and the angular position of the sign transition differs clearly between the two susceptibility models [Fig. 7(c)], confirming that even modest nonlinear corrections are amplified in a regime of steep phase dispersion.

In Fig. 8 we present results for $d = 0.8c/\omega_p$, and find that the nonlinear influence becomes significantly weaker. Small differences between the first-order and third-order susceptibilities remain visible [Fig. 8(a)], but their impact on the reflection imbalance is modest [Fig. 8(b)]. The reflection minimum occurs at very large incidence angles, where the $\cot\theta_i$ factor in Eq. (5) becomes small, geometrically suppressing the transverse displacement. As a result, the PSHE extrema in Fig. 8(c) are strongly reduced and the sign-transition angle shifts only slightly between the two susceptibility models.

Taken together, Figs. 6-8 show that nonlinear susceptibility corrections reshape the same PSHE mechanism established in the linear analysis, mainly through separation-dependent changes in the effective reflection response. In all cases, the reflection minimum appears near the sign transition of the spin Hall shift, confirming that the sign reversal arises from the complex phase-amplitude response of R_p rather than from amplitude suppression alone. Thus, nonlinearity modifies the angular position and strength of the response without changing the basic physical picture. These results establish the PSHE as a highly sensitive probe of nonlinear optical corrections. Importantly, even though the detuning values were intentionally chosen to maximize nonlinear deviations, the perturbative approximation up to third order remains qualitatively accurate, confirming its validity in the weak-excitation regime while highlighting the fundamentally phase-sensitive nature of the spin Hall response. These results therefore define the regime in which the perturbative third-order treatment remains appropriate before stronger-driving effects require the all-orders description examined below.

To further investigate the limitations of perturbative susceptibility descriptions under strong optical driving, we consider the configurations shown in Figs. 9 and 10, corresponding to $d = 0.45c/\omega_p$ and $d = 0.8c/\omega_p$, respectively. In contrast to the weak-excitation regime examined in Figs. 6-8, the probe Rabi frequency is intentionally increased such that the first-order susceptibility exhibits substantially larger deviations from the all-orders susceptibility, reaching amplitude differences of approximately 30% near resonance. Furthermore, for panels (b) and (c) of each figure, the probe detuning is chosen to maximize the difference in the angular position of the PSHE sign transition between the first-order and all-orders solutions.

At $d = 0.45c/\omega_p$, these nonlinear deviations produce clear and experimentally significant consequences. As shown in Fig. 9(a), although

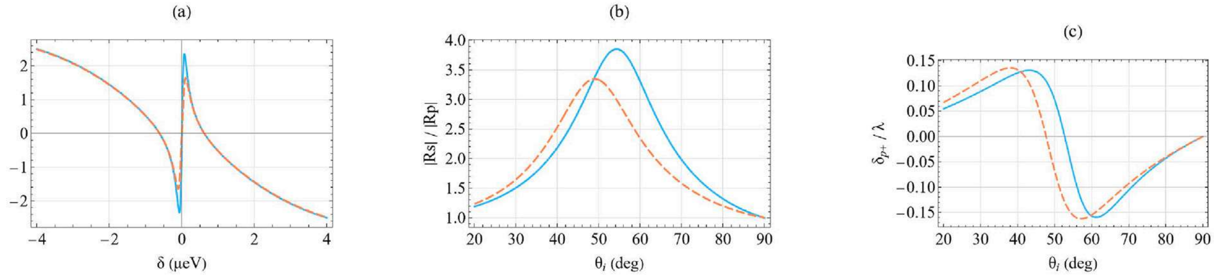

Fig. 6. (a) Re[χ] versus δ, considering the first-order susceptibility $\chi^{(1)}$ (light blue solid curve) and the perturbative effective susceptibility χ_{eff} defined in Eq. (30) (orange dashed curve). The field intensity is chosen such that the third-order approximation closely reproduces the all-orders susceptibility. The corresponding probe Rabi frequency is $\Omega = 0.7\,\Gamma_0$. (b) Reflection-channel imbalance $|R_s|/|R_p|$ versus θ_i at fixed detuning $\delta = 0.05\,\mu$eV. (c) PSHE shift δ_{p+}/λ versus θ_i at the same detuning. Panels correspond to $d = 0.3\,c/\omega_p$ giving $\Gamma_\perp = 8.080\,\Gamma_0$ and $\Gamma_\parallel = 0.015\,\Gamma_0$. The other parameters are the same as in Fig. 2.

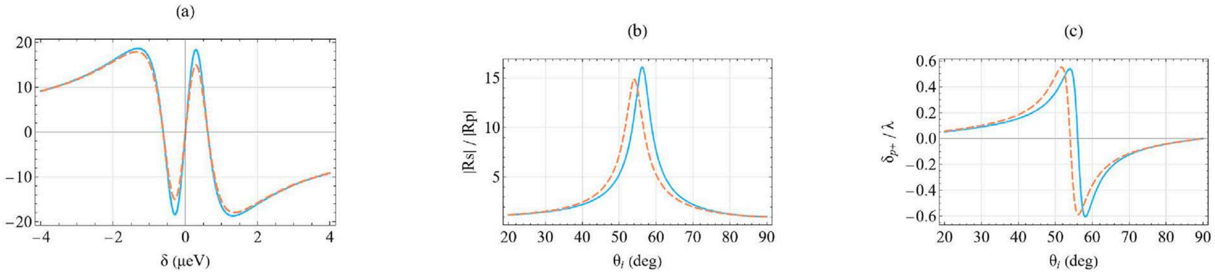

Fig. 7. (a) Re[χ] versus δ, showing the first-order susceptibility $\chi^{(1)}$ (light blue solid curve) and the perturbative effective susceptibility χ_{eff} defined in Eq. (30) (orange dashed curve). The field intensity is chosen such that the third-order approximation closely reproduces the all-orders susceptibility. The corresponding probe Rabi frequency is $\Omega = 0.325\,\Gamma_0$. (b) Reflection-channel imbalance $|R_s|/|R_p|$ versus θ_i at fixed detuning $\delta = 0.05\,\mu$eV. (c) PSHE shift δ_{p+}/λ versus θ_i at the same detuning. Panels correspond to $d = 0.6\,c/\omega_p$ giving $\Gamma_\perp = 1.237\,\Gamma_0$ and $\Gamma_\parallel = 0.0044\,\Gamma_0$. The other parameters are the same as in Fig. 2.

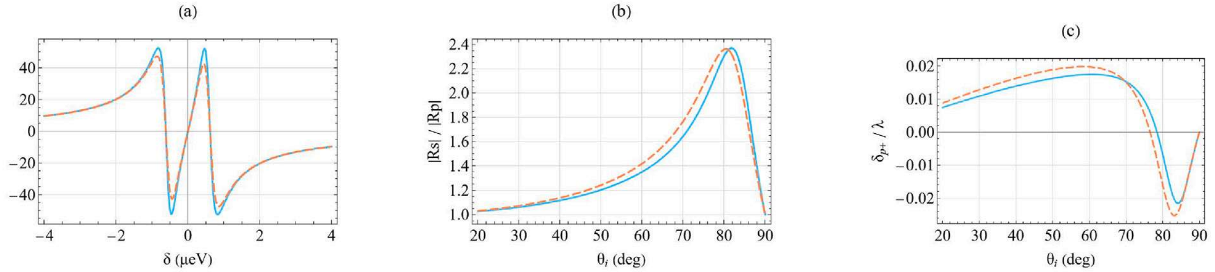

Fig. 8. (a) Re[χ] versus δ, showing the first-order susceptibility $\chi^{(1)}$ (light blue solid curve) and the perturbative effective susceptibility χ_{eff} given by Eq. (30) (orange dashed curve). The field intensity is chosen such that the third-order approximation closely reproduces the all-orders susceptibility. The corresponding probe Rabi frequency is $\Omega = 0.165\,\Gamma_0$. (b) Reflection-channel imbalance $|R_s|/|R_p|$ versus θ_i at fixed detuning $\delta = 0.62\,\mu$eV. (c) PSHE shift δ_{p+}/λ versus θ_i at the same detuning. Panels correspond to $d = 0.8\,c/\omega_p$ giving $\Gamma_\perp = 0.439\,\Gamma_0$ and $\Gamma_\parallel = 0.002\,\Gamma_0$. The other parameters are the same as in Fig. 2.

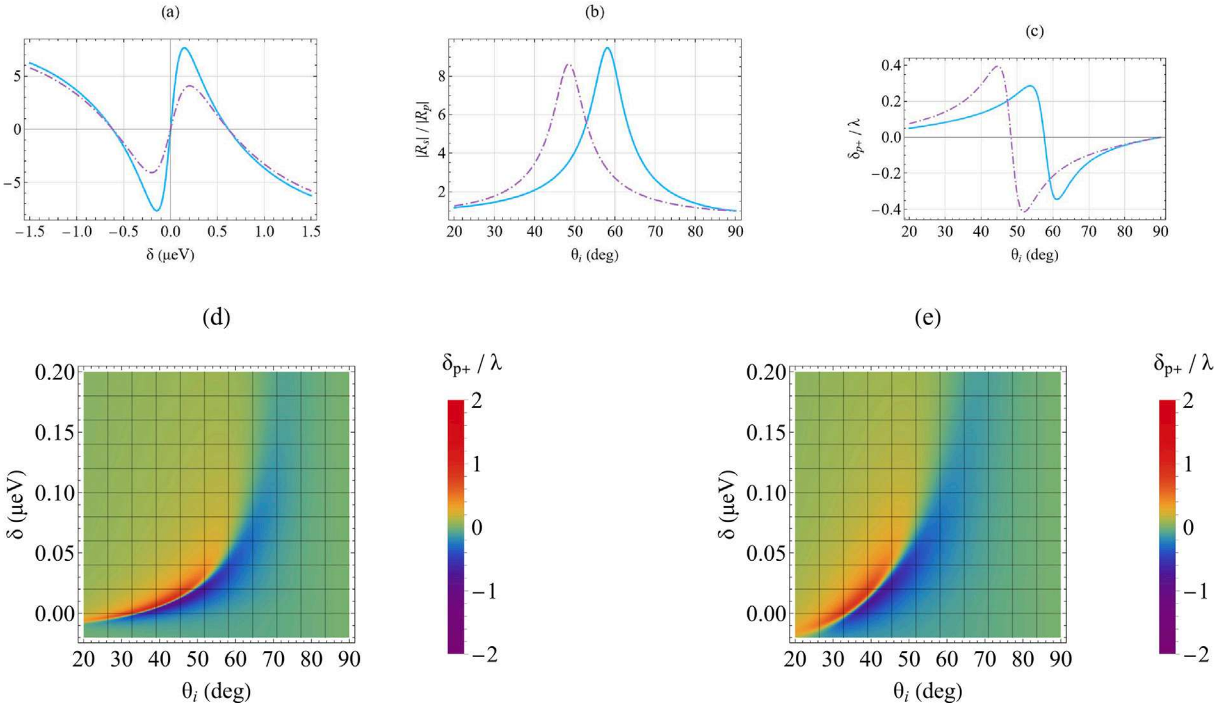

Fig. 9. (a) Re[χ] versus δ, comparing the first-order susceptibility $\chi^{(1)}$ (light blue solid) and the all-orders susceptibility (purple dashed-dotted). The Rabi frequency is $\Omega = 0.860\,\Gamma_0$. (b) Reflection-channel imbalance $|R_s|/|R_p|$ versus θ_i at fixed detuning $\delta = 0.05\,\mu$eV. (c) PSHE shift δ_{p+}/λ versus θ_i at the same detuning. Density map of δ_{p+}/λ in the (θ_i, δ) plane for (d) first-order susceptibility and (e) all-orders susceptibility. Panels correspond to $d = 0.45\,c/\omega_p$ giving $\Gamma_\perp = 0.439\,\Gamma_0$ and $\Gamma_\parallel = 0.002\,\Gamma_0$. The other parameters are the same as in Fig. 2.

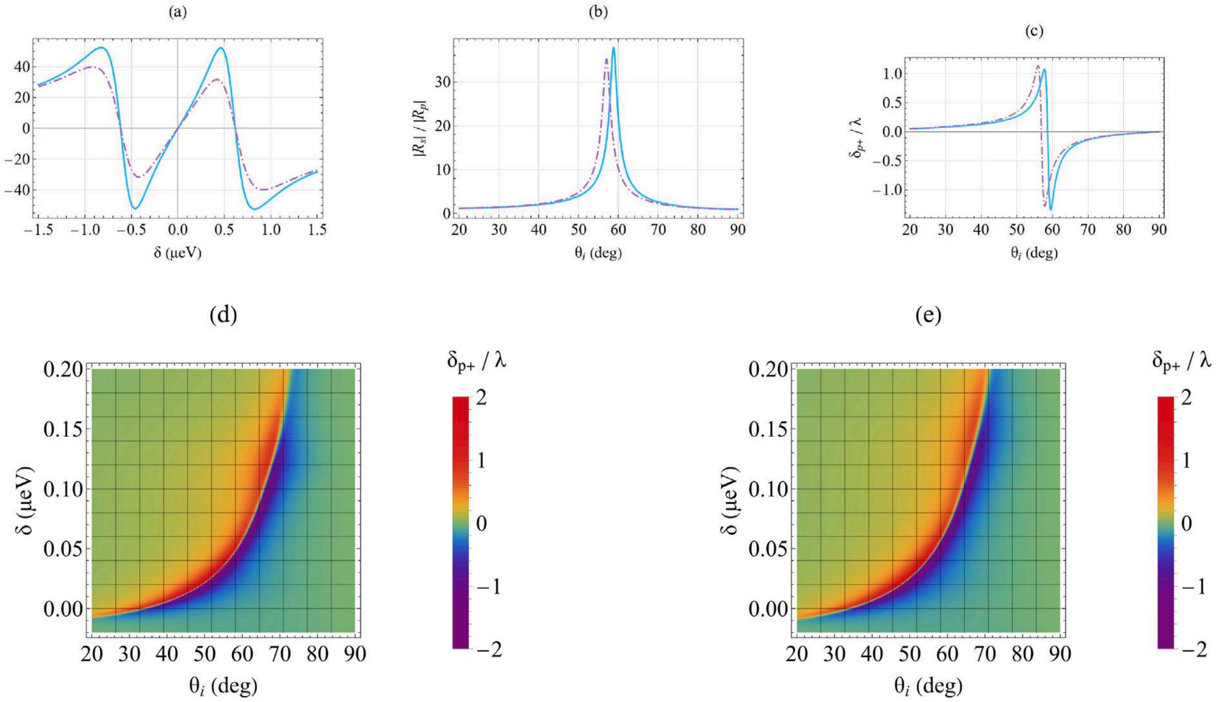

Fig. 10. (a) Re[χ] versus δ, comparing the first-order susceptibility $\chi^{(1)}$ (light blue solid) and the all-orders susceptibility (purple dashed-dotted). The Rabi frequency is $\Omega = 0.312\,\Gamma_0$. (b) Reflection-channel imbalance $|R_s|/|R_p|$ versus θ_i at fixed detuning $\delta = 0.05$ μeV. (c) PSHE shift δ_{p+}/λ versus θ_i at the same detuning. Density map of δ_{p+}/λ in the (θ_i, δ) plane for (d) first-order susceptibility and (e) all-orders susceptibility. Panels correspond to $d = 0.8\,c/\omega_p$ giving $\Gamma_\perp = 0.439\,\Gamma_0$ and $\Gamma_\parallel = 0.002\,\Gamma_0$. The other parameters are the same as in Fig. 2.

the first-order and all-orders susceptibilities retain identical resonance positions and the same overall dispersive structure, the first-order approximation substantially overestimates the resonance amplitude and the steepness of the dispersive slope. Because the reflection coefficient depends directly on the susceptibility through the intracavity permittivity, these spectral discrepancies lead to measurable changes in the angular reflection response. In Fig. 9(b), the reflection-channel imbalance peak shifts toward larger incidence angles in the perturbative model and exhibits a higher maximum value. This shift translates directly into a corresponding displacement of the PSHE sign-transition angle in Fig. 9(c). Importantly, this shift occurs without any change in the resonance position, confirming that nonlinear corrections modify the angular phase-matching condition governing the PSHE rather than the underlying resonance frequency. The density maps in Figs. 9(d) and Fig. 9(e) provide a global view: the zero-displacement contour, which defines the boundary separating positive and negative transverse shifts, follows clearly different trajectories in the first-order and all-orders models across the detuning-angle parameter space. This indicates that under strong driving the first-order approximation does not merely introduce quantitative amplitude errors but alters the phase-sensitive angular structure of the PSHE response itself. The PSHE therefore directly reveals the limitations of low-order susceptibility expansions in the strongly nonlinear regime.

A similar comparison at $d = 0.8c/\omega_p$ is shown in Fig. 10. As in the previous case, the first-order susceptibility overestimates the amplitude of the dispersive features [Fig. 10(a)], leading to measurable differences in the reflection imbalance and PSHE response. However, the resulting phase deviations are significantly smaller than at $d = 0.45c/\omega_p$. The reflection imbalance and PSHE curves in Fig. 10(b) and (c) remain qualitatively similar, and the sign-transition angle shifts by only a few degrees between the first-order and all-order models. This reduced phase sensitivity is further confirmed by the density maps in Fig. 10(d) and (e), where the zero-displacement contours remain much closer throughout the parameter space than in Fig. 9. These results show that the impact of strong excitation on the PSHE depends critically on the phase sensitivity of the reflection response, which is strongly influenced by the emitter-metal coupling geometry: when the phase sensitivity is reduced, first-order descriptions remain qualitatively reliable despite quantitative deviations, whereas accurate prediction in the strongly phase-sensitive regime requires the all-orders susceptibility.

Nonlinear optical corrections do not change the basic PSHE mechanism itself; rather, they modify it indirectly by changing the effective susceptibility, which shifts the reflection minimum, the polarization-channel imbalance, and the phase-sensitive angular condition governing sign reversal.

4. Conclusions

We have theoretically demonstrated coherent spin–orbit control in a hybrid platform where a quantum emitter layer is coupled to a plasmonic interface. Interference between the direct radiative channel and the surface-plasmon-polariton pathway generates plasmon-induced transparency in the probe response, suppresses the p-polarized reflection channel in a resonant angular region, and produces large, sign-reversible Imbert-Fedorov shifts. By varying the emitter–metal separation, the system is tuned across distinct emitter–plasmon hybrid regimes in which both the reflection-amplitude imbalance and the angular dispersion of the complex reflection response are modified. As a result, the magnitude, sign-transition angle, and angular profile of the transverse spin displacement evolve with separation, rather than following a strictly monotonic distance dependence. This behavior reflects the distance-dependent restructuring of the hybrid plasmon–emitter response, shaped by Kramers-Kronig causality and by the SPP-tailored local density of states, with different observables responding differently across the various hybrid regimes.

Beyond the linear regime, nonlinear susceptibility provides an additional control mechanism. Even weak nonlinear corrections can shift the sign-transition angle of the spin Hall displacement, while stronger excitation leads to substantial deviations from perturbative predictions. These results show that the PSHE is sensitive to the full complex optical response of the hybrid system and can therefore serve as a probe of nonlinear light-matter interactions.

Overall, our results provide design-level insight into hybrid spin–orbit photonic functionalities, including spin-dependent beam steering, routing, and phase-sensitive metrology. The proposed mechanism is compatible, at least at the proof-of-principle level, with on-chip architectures employing solid-state emitters coupled to nanofabricated plasmonic arrays, and the predicted displacement could be investigated experimentally through reflection-based, polarization-resolved beam-shift measurements. At the same time, the largest PSHE values predicted in the near-zero-reflection regime should be interpreted as idealized upper-bound estimates rather than directly observable device-level figures of merit. Their practical observability is expected to depend on the trade-off between displacement magnitude and reflected power, as well as on finite beam divergence, angular averaging, alignment stability, detector noise, and measurement sensitivity.

In realistic solid-state implementations, particularly at room temperature, pure dephasing and inhomogeneous broadening can weaken the coherence underlying sharp transparency-like features, thereby broadening the spectral response and reducing the dispersive enhancement of the PSHE. In addition, fabrication tolerances in the nanoshell array, including variations in core radius, shell thickness, lattice spacing, surface roughness, and emitter–surface separation, can modify and broaden the plasmonic resonances, reduce PIT contrast, and smooth the phase-sensitive reflection response. These considerations are expected to reduce both the contrast of the transparency window and the sharpness of the corresponding PSHE extrema under realistic conditions. The present results should therefore be regarded as proof-of-principle theoretical predictions and design guidance, while a device-specific quantitative treatment of realistic losses, dephasing, and fabrication imperfections is left for future experimentally oriented work.

CRediT authorship contribution statement

Muqaddar Abbas: Writing – original draft, Validation, Software, Investigation, Formal analysis. **Spyridon G. Kosionis:** Writing – original draft, Validation, Software, Methodology, Formal analysis. **Vassilios Yannopapas:** Writing – review & editing, Validation, Investigation, Formal analysis. **Emmanuel Paspalakis:** Writing – review & editing, Supervision, Investigation, Conceptualization. **Hamid R. Hamedi:** Supervision, Methodology, Investigation, Conceptualization.

Declaration of competing interest

The authors declare that they have no known competing financial interests or personal relationships that could have appeared to influence the work reported in this paper.

Data availability

Data will be made available on request.

References

[1] M. Fleischhauer, A. Imamoglu, J.P. Marangos, Rev. Mod. Phys. 77 (2005) 633.
[2] W.L. Barnes, A. Dereux, T.W. Ebbesen, Nature 424 (2003) 824.
[3] B. Luk'yanchuk, N.I. Zheludev, S.A. Maier, N.J. Halas, P. Nordlander, H. Giessen, C.E. Chong, Nat. Mater. 9 (2010) 707.
[4] S. Zhang, D.A. Genov, Y. Wang, M. Liu, X. Zhang, Phys. Rev. Lett. 101 (2008) 047401.
[5] R.W. Boyd, J. Mod. Opt. 56 (2009) 1908.
[6] Z. Zhang, J. Yang, T. Du, X. Jiang, Carbon 190 (2022) 80.
[7] Z. Zhang, J. Yang, X. He, Y. Han, J. Huang, D. Chen, J. Phys. D Appl. Phys. 53 (2020) 315101.
[8] S. Evangelou, V. Yannopapas, E. Paspalakis, Phys. Rev. A 86 (2012) 053811.
[9] S. Evangelou, V. Yannopapas, E. Paspalakis, Phys. Rev. A 83 (2011) 023819.
[10] F. Carreño, M.A. Antón, V. Yannopapas, E. Paspalakis, Phys. Rev. B 95 (2017) 195410.
[11] H.R. Hamedi, V. Yannopapas, E. Paspalakis, Annalen der Physik 533 (2021) 2100117.
[12] H.R. Hamedi, V. Yannopapas, G. Juzeliūnas, E. Paspalakis, Phys. Rev. B 106 (2022) 035419.
[13] H.R. Hamedi, V. Yannopapas, E. Paspalakis, J. Ruseckas, Results Phys. 54 (2023) 107135.
[14] H.R. Hamedi, V. Kudriašov, S.H. Asadpour, V. Yannopapas, E. Paspalakis, J. Ruseckas, Phys. Rev. B 111 (2025) 035415.
[15] H. Chen, J. Ren, Y. Gu, D. Zhao, J. Zhang, Q. Gong, Sci. Rep. 5 (2016) 18315.
[16] J. Ren, H. Chen, Y. Gu, D. Zhao, H. Zhou, J. Zhang, Q. Gong, Nanotechnology 27 (2016) 425205.
[17] S.H. Asadpour, H.R. Soleimani, J. Appl. Phys. 119 (2016) 023102.
[18] K.Y. Bliokh, F.J. Rodríguez-Fortuño, F. Nori, A.V. Zayats, Nat. Photonics 9 (2015) 796.
[19] M. Onoda, S. Murakami, N. Nagaosa, Phys. Rev. Lett. 93 (2004) 083901.
[20] K.Y. Bliokh, Y.P. Bliokh, Phys. Rev. Lett. 96 (2006) 073903.
[21] J. Sinova, S.O. Valenzuela, J. Wunderlich, C. Back, T. Jungwirth, Rev. Mod. Phys. 87 (2015) 1213.
[22] K.Y. Bliokh, A. Aiello, J. Opt. 15 (2013) 014001.
[23] O. Hosten, P. Kwiat, Science 319 (2008) 787.
[24] X. Zhou, Z. Xiao, H. Luo, S. Wen, Phys. Rev. A 85 (2012) 043809.
[25] F. Cardano, L. Marrucci, Nat. Photonics 9 (2015) 776.
[26] L. Cai, M. Liu, S. Chen, Y. Liu, W. Shu, H. Luo, S. Wen, Phys. Rev. A 95 (2017) 013809.
[27] S. Chen, X. Zhou, C. Mi, H. Luo, S. Wen, Phys. Rev. A 91 (2015) 062105.
[28] A. Aiello, N. Lindlein, C. Marquardt, G. Leuchs, Phys. Rev. Lett. 103 (2009) 100401.
[29] X. Yin, Z. Ye, J. Rho, Y. Wang, X. Zhang, Science 339 (2013) 1405.
[30] P. Dong, J. Xu, J. Cheng, Phys. Plasmas 31 (2024) 012103.
[31] X. Ling, X. Zhou, K. Huang, Y. Liu, C.-W. Qiu, H. Luo, S. Wen, Rep. Prog. Phys. 80 (2017) 066401.
[32] L. Sheng, H. Luo, S. Wen, Phys. Rep. 1014 (2023) 1.
[33] S. Liu, S. Chen, S. Wen, H. Luo, Opto-electron. Sci. 1 (2022) 220007.
[34] M. Kim, D. Lee, T.H. Kim, Y. Yang, H.J. Park, J. Rho, Nat. Photonics 16 (2022) 258.
[35] X. Zhou, X. Ling, IEEE Photonics J. 8 (1) 2016.
[36] X.-J. Tan, X.-S. Zhu, Opt. Lett. 41 (2016) 2478.
[37] Y. Xiang, X. Jiang, Q. You, J. Guo, X. Dai, Photon. Res. 5 (2017) 467.
[38] L. Salasnich, Phys. Rev. A 86 (2012) 055801.
[39] X. Yu, X. Wang, Z. Li, L. Zhao, F. Zhou, J. Qu, J. Song, Nanophotonics 10 (2021) 3031.
[40] N.I. Petrov, Y.M. Sokolov, V.V. Stoiakin, V.A. Danilov, V.V. Popov, B.A. Usievich, 2024, arXiv preprint arXiv:2408.13151.
[41] Q. Liu, X. Zhao, F. Li, S. Chen, Opt. Lett. 46 (2021) 2537.
[42] O. You, B. Bai, X. Wu, Z. Zhu, Q. Wang, Nanophotonics 12 (2023) 1159.
[43] F. Badshah, I. Boukhris, M.S. Al-Buriah, Y. Zhou, M. Idrees, Ziauddin, 2025, arXiv preprint arXiv:2509.03844.
[44] F. Badshah, D.-Y. Lü, J. Xie, Z. Shi, Q. He, M. Idrees, Opt. Laser Technol. 192 (2025) 113816.
[45] M. Abbas, G. Din, H.R. Hamedi, P. Zhang, Phys. Rev. A 111 (2025) 053716.
[46] S. Xiao, J. Wang, F. Liu, S. Zhang, X. Yin, J. Li, Nat. Commun. 6 (2015) 8360.
[47] V. Kumar, A. Kumar, R. Srivastava, A.K. Sharma, Y.K. Prajapati, IEEE J. Quantum Electron. 61 (1) 2025.
[48] V. Kumar, J.B. Maurya, Y.K. Prajapati, IEEE J. Sel. Top. Quantum Electron. 31 (1) 2025.
[49] V. Kumar, R. Srivastava, Y.K. Prajapati, IEEE Sens. J. 23 (2023) 20976.
[50] V.A. Popescu, Y.K. Prajapati, A.K. Sharma, IEEE Trans. Magn. 57 (1) 2021.
[51] Y.K. Prajapati, J.B. Maurya, A.K. Sharma, J. Phys. D Appl. Phys. 55 (2022) 095102.
[52] G.M. Akselrod, C. Arber, J. Huang, T.B. Hoang, P.T. Bowen, L. Su, D.R. Smith, M.H. Mikkelsen, Nat. Photonics 8 (2014) 835.
[53] R. Chikkaraddy, B. de Nijs, F. Benz, S.J. Barrow, O.A. Scherman, E. Rosta, A. Demetriadou, P. Fox, O. Hess, J. J. Baumberg, Nature 535 (2016) 127.
[54] S. Evangelou, V. Yannopapas, E. Paspalakis, J. Mod. Opt. 61 (2014) 1458.
[55] R.-G. Wan, M.S. Zubairy, Phys. Rev. A 101 (2020) 033837.
[56] J. Wu, J. Zhang, S. Zhu, G.S. Agarwal, Opt. Lett. 45 (2019) 149.
[57] M. Waseem, M. Shah, G. Xianlong, Phys. Rev. A 110 (2024) 033104.
[58] M. Abbas, P. Zhang, H.R. Hamedi, Phys. Rev. A 111 (2025) 043708.
[59] M. Abbas, Y. Wang, F. Wang, H.R. Hamedi, P. Zhang, Chaos Solitons Fractals 196 (2025) 116292.
[60] M. Shah, S. Qamar, M. Waseem, Opt. Express 33 (2025) 39359.
[61] F. Badshah, D. Y. Lü, J. Xie, Z. Shi, Q. He, M. Idrees, Opt. Laser Technol. 192 (2025) 113816.